

AGCM hindcasts with SST and other forcings: Responses from global to agricultural scales

Kathryn Pierce Shah, David Rind,¹ Leonard Druryan, Patrick Lonergan,² and Mark Chandler

Center for Climate Systems Research, Columbia Earth Institute, Columbia University, NASA Goddard Institute for Space Studies, New York

Abstract. Multiple realizations of the 1969–1998 time period have been simulated by the GISS AGCM to explore its responsiveness to accumulated forcings, particularly over sensitive agricultural regions. A microwave radiative transfer postprocessor has produced the AGCM lower tropospheric, tropospheric, and lower stratospheric brightness temperature (T_b) time series for correlations with microwave sounding unit (MSU) time series. AGCM regional surface air temperature and precipitation were also correlated with GISTEMP temperature data and with rain gage data. Seven realizations by the AGCM were forced solely by observed sea surface temperatures. Subsequent runs hindcast January 1969 through April 1998 with an accumulation of forcings: observed sea surface temperatures (SSTs), greenhouse gases, stratospheric volcanic aerosols, stratospheric and tropospheric ozone, and tropospheric sulfate and black carbon aerosols. Lower stratospheric T_b correlations between the AGCM and the MSU for 1979–1998 reached as high as 0.93 globally given SST, greenhouse gases, volcanic aerosol, and stratospheric ozone forcings. Midtropospheric T_b correlations reached as high as 0.66 globally and 0.84 across the equatorial, 20°S–20°N band. Oceanic lower tropospheric T_b correlations were less high at 0.59 globally and 0.79 across the equatorial band. Of the sensitive agricultural areas considered, Nordeste in northeastern Brazil was simulated best with midtropospheric T_b correlations up to 0.80. The two other agricultural regions, in Africa and in the northern midlatitudes, suffered from higher levels of non-SST-induced variability. Zimbabwe had a maximum midtropospheric correlation of 0.54, while the U.S. Corn Belt reached only 0.25. Hindcast surface temperatures and precipitation were also correlated with observations, up to 0.46 and 0.63, respectively, for Nordeste. Correlations between AGCM and observed time series improved with addition of certain atmospheric forcings in zonal bands but not in agricultural regions encompassing only six AGCM grid cells.

1. Introduction

The extreme El Niño of 1998 has spurred research and funding agencies to sponsor cross-disciplinary work on climate effects, particularly on agricultural, societal, and economical impacts. The Climate, Agriculture, Fisheries and Environment (CAFE) group at the Goddard Institute for Space Studies (GISS), Goddard Space Flight Center (GSFC), and Lamont-Doherty Earth Observatory (LDEO) has hindcasts of the 1969–1998 period from an AGCM initially forced with observed sea surface temperatures (SSTs) and then with additional atmospheric forcings. The goal is to optimize hindcasting over agricultural regions sensitive to El Niño events, drive off-line agricultural, fishery, and economic models and begin to integrate a forecasting sea surface temperature model. One of the initial steps is to gauge the AGCM involved and to determine agricultural regions that could have successful forecasts.

Correct temperature and precipitation over the agricultural

regions are needed to drive crop models. Three dissimilar agricultural regions are considered here: Nordeste in northeastern Brazil, neighboring the tropical Pacific forcing of El Niño–Southern Oscillation (ENSO), Zimbabwe in southern Africa, distanced by a continental landmass and the Atlantic Basin from ENSO forcing, and the U.S. Corn Belt, in the highly variable northern midlatitudes. *Chu* [1991] has detailed ENSO-related droughts and famines over Nordeste. *Cane et al.* [1994] have correlated the Zimbabwe maize yield production to ENSO SSTs, while *Phillips et al.* [1999] examined correlations of regional U.S. Corn Belt data to ENSO SSTs. The responses and teleconnections of AGCM due to SST and other forcings are assessed herein primarily with the microwave sounding unit (MSU) brightness temperature (T_b) data (see Figure 1) but also with the GISS global surface air temperature analyses (GISTEMP) and with regional rain gage observations.

Deep convection over warm, tropical SST forcing in a climate model is translated into a change in the tropical upper troposphere and then translated into an extratropical tropospheric response. *Boyle* [1998] argues that different mean states of an AGCM will affect the extratropical responses to tropical SSTs through varying planetary wave propagation and mean winds. *Tribbia* [1991] discusses a nonlinear dependence of the extratropical response on the subtropical jet strength and position. *Yulaeva and Wallace* [1994] warn that some

¹NASA Goddard Institute for Space Studies, Goddard Space Flight Center, New York.

²Science Systems and Applications, New York.

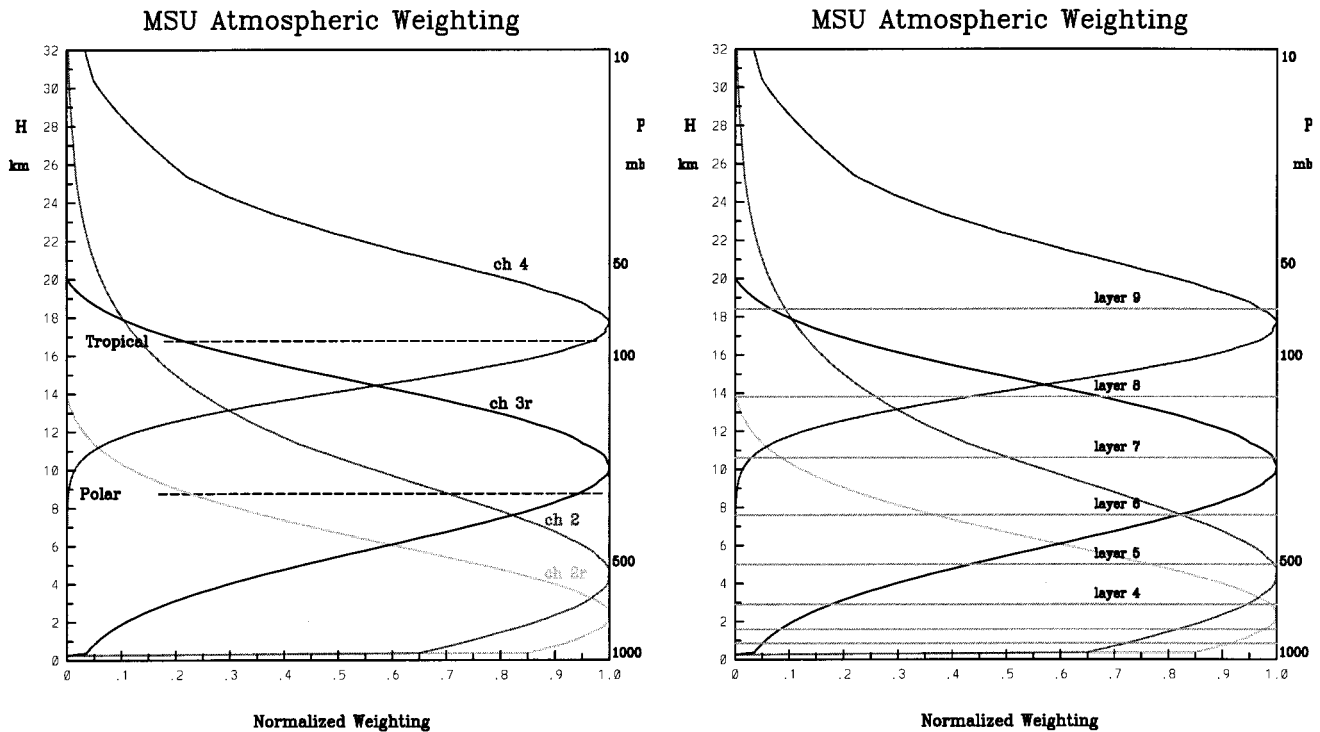


Figure 1. Microwave sounding unit (MSU) channel weighting functions over a land surface emissivity of 1.0 and from a 1976 Standard Atmosphere equivalent to a mean annual, midlatitude atmosphere are displayed relative to typical tropical and polar tropopause levels (left) and to the nine vertical layers of the atmospheric general circulation model (AGCM) (right). AGCM channel T_b is calculated via radiative transfer in this work.

GCMs, dominated by baroclinic adjustment for dispersal of excess tropical warmth, will not create teleconnections correctly. They outline the necessary simulation of observed reduced static stability for the upper troposphere equatorward of the jet streams due to the El Niño–warmed tropical troposphere. This reduced static stability would enhance the potential vorticity across the subtropical jet streams and strengthen them. The Hadley cell could be amplified by increased tropical uplift and provide the needed eastward acceleration to the jet streams. Concurrently, the lower stratospheric pressures should undergo observed zonal mean cooling with uplift of the tropopause and negative correlations with warmed SSTs. With inclusion of volcanic and tropospheric aerosols and variable ozone distribution forcings, the CAFE AGCM may combine radiative and dynamical conditions needed to communicate the tropical SST forcing to higher latitudes. (This also relates to two schools of thought on the source of stratospheric trends wherein either radiative impacts from ozone loss explain the lower stratospheric cooling or whether circulation changes driven by alteration of the troposphere and, perhaps, greenhouse gases are necessary.)

This exploration of the performance of a typical climate model forced by known atmospheric and sea surface temperature events at global, zonal, and regional levels uses a nine-vertical-layer version of the GISS AGCM (Figure 1) with a 4° latitude by 5° longitude resolution. The coarse resolution of this AGCM makes the needed computer time for multiple transient runs bearable. The initial seven AGCM runs were only forced by observed SSTs. Subsequent individual runs, still forced at the lower boundary by observed SSTs, added in changing greenhouse gases, volcanic aerosol opacities, lower

stratospheric and tropospheric ozone, and tropospheric black carbon and sulfate aerosols through April 1998 (see Table 1 and the Appendix). This coarse resolution model has performed extremely well in climate model comparisons to observations, being tied for the top U.S. climate model and fifth out of 29 models in an AMIP examination of the hydrological cycle, for example [Lau *et al.*, 1996].

The goal of optimizing hindcasting, as defined as a near-unity correlation between an AGCM and an observed time series, has obstacles. Neither an ensemble of AGCM realizations nor a data set is perfect. First, the year 1998 has produced numerous papers on calibration and processing concerns with the MSU data [Wentz and Schabel, 1998; Hurrell and Trenberth, 1998; Prabhakara *et al.*, 1998; Gaffen, 1998; Hansen, 1998; Wu and McAvaney, 1998]. Several versions of the MSU data are publically available, as criticisms are addressed and as longer baselines become available [Christy *et al.*, 1998]. Second, an AGCM may produce a good simulation by chance, so multiple simulations are necessary in order to assess a potential of correct hindcasting. Yet how many simulations are appropriate for a particular model? How should this compare with the real world, in which only one actual realization took place? The AGCM's own internal variability sources can prompt extratropical responses that overpower teleconnections from the tropics associated with ENSO. Boyle [1998] refers to this as “the chaotic nature of the midlatitude dynamics.” Third, this AGCM was forced by observed AMIP I SSTs, volcanic aerosol opacities, ozone levels, and tropospheric aerosols each of which has its own weaknesses. Fourth, an AGCM simulation of an anomaly is likely to be dependent on its mean-observation-based parameterizations and its mean climate.

Table 1. AGCM Transient Experiments

AGCM Run	Description
Control	control run, mean SSTs
<i>SST Forcing</i>	
SST a	obs sea surface temperatures
SST b	obs sea surface temperatures
SST c	obs sea surface temperatures
SST d	obs sea surface temperatures
SST e	obs sea surface temperatures
SST f	obs sea surface temperatures
SST g	obs sea surface temperatures
<i>SST Ensemble</i>	
SST ac	average of three runs, SSTa–SSTc
SST ae	average of five runs, SSTa–SSTe
SST ag	average of seven runs, SSTa–SSTg
<i>Atmospheric Forcing</i>	
GG	obs SSTs + CO ₂ and trace gases
VOL	obs SSTs + CO ₂ and trace gases + volcanic aerosols
O3s	obs SSTs + CO ₂ and trace gases + volcanic aerosols + ΔO ₃ strat
O3t	obs SSTs + CO ₂ and trace gases + volcanic aerosols + ΔO ₃ trop
O3	obs SSTs + CO ₂ and trace gases + volcanic aerosols + ΔO ₃ strat and trop
O3sS	obs SSTs + CO ₂ and trace gases + volcanic aerosols + ΔO ₃ strat + trop sulfate aerosols
O3sSC	obs SSTs + CO ₂ and trace gases + volcanic aerosols + ΔO ₃ strat + trop sulfate and carbon aerosols
O3SC	obs SSTs + CO ₂ and trace gases + volcanic aerosols + ΔO ₃ strat and trop + trop sulfate and carbon aerosols

Hopefully, the following analysis of these multiple AGCM simulations can begin to answer some of these questions:

1. Does the AGCM simulate the midtropospheric temperature dumbbell pattern of *Yulaeva and Wallace* [1994] in response to El Niño SST forcing? Does the AGCM tropopause rise and the lower stratospheric channel 4 temperatures cool in localized response to tropospheric warmth during El Niño [Reid *et al.*, 1989; *Yulaeva and Wallace*, 1994; *Randel and Cobb*, 1994]?
2. Is there reduced static stability in the tropical upper troposphere over the Pacific due to warm equatorial SST? Do the upper tropospheric, subtropical jet streams, and the Hadley cell circulation strengthen promoting teleconnections?
3. How well can the AGCM correlate with the oceanic lower tropospheric, midtropospheric, and lower stratospheric temperature time series of MSU? Do the correlations improve with additional atmospheric forcings?
4. How good is the AGCM response over sensitive agricultural regions? Does the AGCM response over these agricultural regions improve with inclusion of atmospheric forcings?
5. How many simulations are useful?

Section 2 examines the AGCM upper air temperatures, the simulated monthly mean climate, and variability. Section 3 looks at AGCM zonal responsiveness to ENSO and other forcings in terms of diagnostic maps and correlations to MSU time series. Section 4 focuses on the agricultural region responsiveness to SST and additional atmospheric forcings via the MSU, GISTEMP, and precipitation observations. Section 5 concludes this paper with replies to the above questions, further discussion, and future work planned. The Appendix describes the AGCM, the applied forcings for the individual

transient runs, and the off-line microwave radiative transfer model.

2. AGCM Lower Stratospheric and Tropospheric Means

As discussed by *Boyle* [1998], perhaps the very different mean states of the initial atmosphere will affect the extratropical responses to tropical SSTs due to varying planetary wave propagation and mean winds. *Tribbia* [1991], for instance, discusses the nonlinear dependence of the extratropical response on the subtropical jet strength and position. *Kiladis and Diaz* [1986] documented observational evidence of midlatitude teleconnections in terms of the Aleutian Low magnitude during the winter of 1983. *Hoerling and Kumar* [1997] and *Hoerling et al.* [1997] also detail wave trains which shape teleconnections during ENSO events. Such dynamical responses and background wind profiles will be dependent on the background temperature structure.

A 10-year average from the AGCM control run produced tropospheric temperatures in good agreement with the MSU mean climatology (Plate 1). The AGCM used mean SSTs from AMIP data over the 1982–1987 period and mean ice coverage from the 1979–1993 period as a lower boundary. The resultant lower, middle, and upper tropospheric temperatures generally match MSU observations but are too cool over the middle to high latitudes by several degrees. Lower tropospheric T_b are also significantly cool over the equatorial oceans (based on ratios to MSU interannual standard deviations in Plate 1). These weaknesses may be related to insufficient high cloud coverage in the northern latitudes and insufficient upper tropospheric atmospheric moisture, both of which are difficult to confirm. This tropical lower tropospheric coolness and higher latitude tropospheric coldness are common, tenacious flaws in AGCMs [IPCC, 1996]. In terms of impacts on the subtropical jets, the latitudinal temperature gradients in the midtropospheric T_b , which influence the strength of the jets, are only slightly amplified (Plate 1).

The lower stratosphere of the AGCM exhibits more notable weaknesses. The presence of the model top at 10 mbar and the lack of gravity wave parameterizations in the model distort the annual cycle of mean temperatures. The AGCM T_b values differ from MSU observations by over 10° over the Southern Pole and at wave centers and differ by several degrees over the tropics. The excess tropical warmth in the lower stratosphere is another common, unwelcome AGCM flaw [IPCC, 1996]. *Rind et al.* [1999] detail the need for gravity wave parameterizations and a high altitude for the model top in order to correctly simulate the lower stratosphere. Currently, the low height of the model top (at 10 mbar or roughly 32 km) reflects energy back into the troposphere. This artificial, unavoidable top had originally set up strong wind and temperature deviations in early nine-layer GCMs [Hansen *et al.*, 1983]. As a solution, a specified stratospheric drag was placed in the top vertical layer to bring wind and temperature deviations down to acceptable levels. However, this artificial drag in the top layer of the model sets up divergence over the summer pole and convergence over the winter pole and in the meridional and vertical upper layer winds. Unrealistic conditions near the model top may affect tropospheric features and impact the AGCM teleconnections; this aspect will be explored in a subsequent paper.

Examination of the AGCM mean tropospheric temperature variability from a typical SST-forced run does find appropriate,

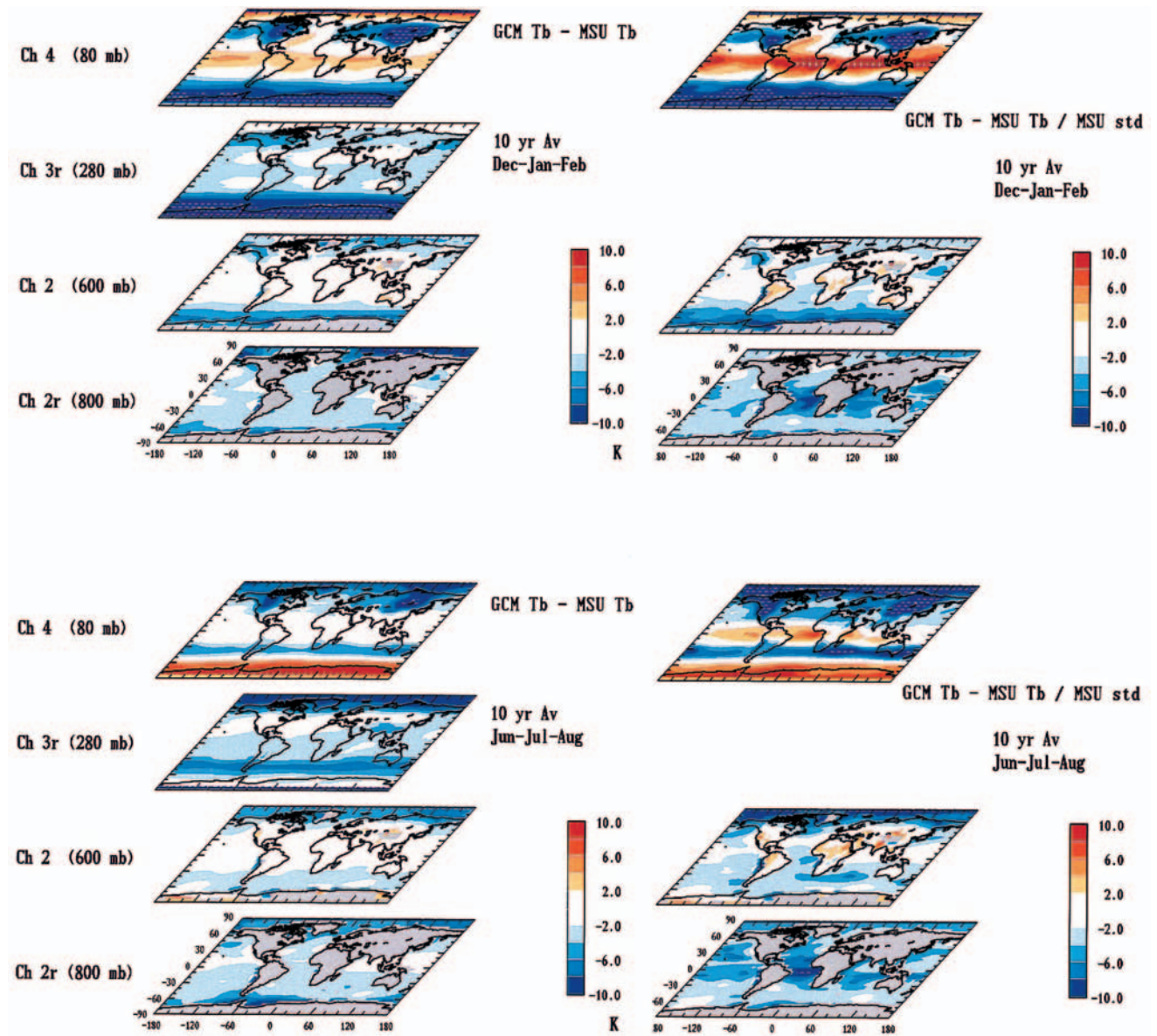


Plate 1. AGCM mean T_b departures from MSU in the lower troposphere up into the lower stratosphere are shown for December-January-February and June-July-August averages (left) and scaled by the observed MSU interannual variability (right). The AGCM control run has climatological sea surface temperatures (SSTs) and sea ice for specified forcings. The upper tropospheric MSU channel 3R values are adjusted to match National Centers for Environmental Protection/National Center for Atmospheric Research (NCEP/NCAR) values as detailed by *Shah and Rind* [1998]. Note regions of inappropriate vertical static stability do occur systematically in the AGCM.

Mid Trop Ch2 Tb Variability

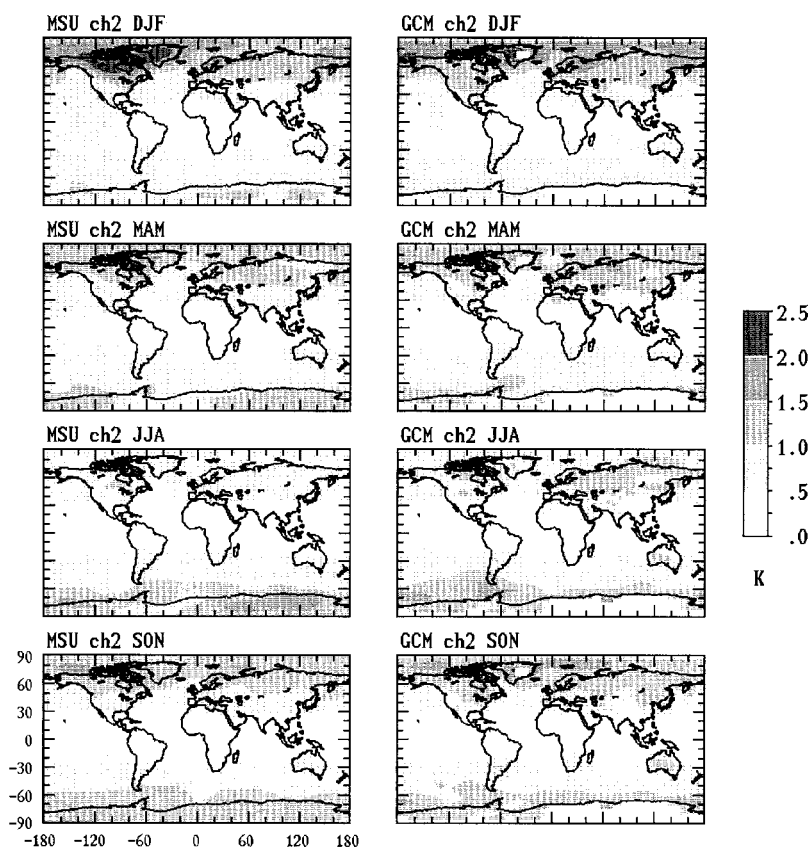


Figure 2. MSU and AGCM seasonal midtropospheric temperature variabilities come from AGCM run SST f, forced only by observed SSTs and from the 1980–1997 period. The MSU anomalies are from the version “c” of that data.

stronger variability over high latitudes, winter seasons, and continents. This is despite the use of climatological SSTs, which reduces variability over the oceans. Figure 2 shows the seasonal maps of MSU and AGCM variability over the 1980–1997 period. The MSU midtropospheric temperatures have several tenths of a degree more variability over the equatorial Pacific and over northern landmasses during the winter (DJF) and spring (MAM). The AGCM actually produces too much midtropospheric variability over the continental United States during the northern winter and over the Asian continent during the northern summer (JJA).

The difficulties noted above also affect the lower stratospheric variability of the model. Placement of variability in the AGCM (not shown) is appropriate with maxima over the northern winter high latitudes and minima across the equatorial latitudes. The AGCM lower stratosphere does not have wave-related variability at middle to high latitudes in both the Northern and the Southern Hemispheres. The MSU maps also show more variability over the northern winter pole from sudden stratospheric warmings. (Sudden stratospheric warmings are simulated in the 23-layer version of this AGCM with a model top above the stratopause.) Consequently, the nine-layer AGCM lower stratospheric variability peaks at 4 K when MSU observations peak at nearly 8 K in winter over northern high latitudes.

3. AGCM Spatial and Time Series Responses

The responses of the AGCM to SST and accumulated forcings are examined in terms of anomaly maps and time series correlations from global to regional scales. Warm ENSO SST anomalies should prompt strong precipitation and deep convection over the eastern equatorial Pacific, strengthen the Hadley cell and the subtropical jets; induce changes to the static stability of the tropical troposphere, create warm (cold) centers of tropospheric (stratospheric) temperature anomalies, and spur extratropical teleconnections. These teleconnections may or may not be properly engaged and positioned in order to spur temperature and precipitation impacts over sensitive agricultural regions in the AGCM.

The monthly-mean T_b baseline of 1982–1991 was used for the tropospheric channels, while 1984–1990 was used for the lower stratospheric channel to match MSU version “c” baselines. The AGCM control run supplies the baseline for the SST-forced runs, while individual atmospheric forcing runs supply their own baselines (see Table 1). Maps of T_b anomalies or AGCM diagnostics are monthly anomalies without any smoothing applied. Correlations are between 3-month-smoothed AGCM and MSU time series to emphasize the low-frequency component of the climate response.

Tables of correlations have specializations. Parentheses de-

note when a correlation is more than 2 standard deviations away from the mean correlation of the seven SST runs. Then that AGCM run is deemed significantly different from the population of the SST runs. Brackets denote when a correlation significantly differs from another correlation based on a Fisher z -test. The difference between two individual correlations is deemed significant herein if the associated Fisher significance is greater than 95% for z values from the 3-month-smoothed time series and greater than 80% for z values from unsmoothed time series (see *Press et al.* [1989] for further discussion). Fisher z -test comparisons are between a run with a new forcing and a preceding run without that forcing: run GG correlation is compared to the mean SST correlation, run VOL to run GG, runs O3s, O3t, and O3 to run VOL, run O3sS to run O3s, run O3sSC to run O3sS, and run O3SC to run O3sSC. So while one test (parentheses) compares an individual forcing run to the suite of SST runs, the second test (brackets) compares one forcing-combination run to another forcing-combination run.

3.1. Spatial Anomalies, January 1983 and January 1998

Spatial anomalies from a single, SST-forced AGCM run are compared to the real world inherently single realization of El Niño winters during the 1980s. Plate 2 shows changes to AGCM sea surface temperatures, precipitation, and sea level pressure, to AGCM and MSU tropospheric and lower stratospheric temperatures, and to AGCM and GISTEMP surface temperatures for January 1983 and January 1998. These months were selected due to the size of the warm SST anomalies over the eastern Pacific cold tongue (see *Hoerling et al.* [1997] on ENSO nonlinearities). Also, these winter months are characterized with stronger teleconnections to the northern extratropics given the more favorable temperature gradient [see *Trenberth*, 1991].

AGCM sea level pressures in Plate 2a do shift during these El Niño months with decreases over the eastern Pacific and increases over the tropical South Pacific Ocean. As anticipated, the very warm SST anomalies prompt precipitation increases over the eastern equatorial Pacific in the AGCM. The AGCM maximum precipitation anomalies over the eastern Pacific appears concentrated more tightly over latitude than normal, and precipitation diminishes over the southeastern Pacific.

There is associated strengthening of the AGCM northern winter Hadley cell and subtropical jet as detailed in Table 2. During January 1983 and January 1998 the winter Hadley cell strengthens and vertical motion increases by 300% in its southern branch uplift. Its upper tropospheric meridional winds and column stream function concentrate about an 8°N center and increase. The AGCM subtropical jet strengthens by 2.0 m/s in January 1983 and 4.2 m/s in January 1998.

Concurrently, local compensation and cooling in response to movement of the tropopause can be seen in both the MSU and the AGCM lower stratospheric T_b . These T_b values are essentially an integrated temperature across a broad pressure layer, and lifting of the tropopause brings cooler temperatures into the peak sensitivity of channel 4. Changes to the tropical troposphere static stability create warm (cold) centers of tropospheric (stratospheric) temperature anomalies (see Plate 2b). The AGCM could not generate the widespread cooling of lower stratospheric T_b due mostly to ozone depletion since it was only forced by SSTs. MSU observations also show east-west gradients to the midtropospheric warming and lower

stratospheric cooling across the Pacific. This gradient is also present in the maps of the AGCM T_b . The “dumbbell-shaped” centers of warming and cooling straddling the equator over the eastern Pacific in the MSU maps, however, are not always discrete in the AGCM T_b maps. The AGCM also can generate discrete, cool lower stratospheric peaks while not having discrete warm peaks in its midtropospheric T_b .

Over the North Pacific, *Kiladis and Diaz* [1986] documented the enhancement and southward displacement of the Aleutian Low pressure system due to the northward flux of angular momentum during January 1983. The deeper center moved the North Pacific storm systems southward, bringing hard winter storms to the western U.S. coast. The intense strength of the Aleutian Low reached sea level pressure anomalies of -20 mbar, while the AGCM run in Plate 2a reaches anomalies of -14 mbar southwest of Alaska. The associated, observed decrease of sea level pressures over the Greenland Sea and increase of pressures for the Azores High, which led to milder winters over western Europe, are not apparent in the AGCM winter sea level pressure anomalies. So while both observed surface temperature anomaly maps and AGCM hindcasts show warmer conditions over western Europe, they disagree over the Greenland Sea, Arctic Ocean, and northern Asia (Plate 2c). (Milder European winters and associated local surface pressure anomalies do occur if a full stratospheric GCM is used [see *Shindell et al.*, 1999].) Observations and the AGCM hindcast also disagree in terms of surface temperature anomalies in January 1983 and 1998 over North America. Thus while tropical tropospheric and surface changes in the AGCM do occur, it is uncertain if the AGCM creates all the extratropical teleconnections sufficient for responses over extratropical agricultural regions. It is likely that other individual AGCM runs will vary in their spatial responses relative to maps from this single run.

3.2. Midtropospheric Temperature Time Series

Time series of T_b anomalies for 1979–1998, comparable to the period observed by MSU, were calculated first from the seven AGCM transient SST a–SST f runs (see Table 1). These seven runs are identically forced by observed SSTs but differ in terms of initial conditions. They provide a rough range of model internal variability over the examined latitudinal zones and the agricultural regions. Figure 3 shows the 3-month-smoothed MSU midtropospheric channel 2 T_b time series for the equatorial Pacific (20°S–20°N and 80°W–100°E), the AGCM T_b time series from the average of the seven runs, and the range of the individual AGCM time series for each month. These midtropospheric MSU and AGCM channel 2 anomalies clearly capture the warming and coolings of the troposphere due to ENSO events in the 1980s and 1990s. However, Figure 3 also shows the scatter of AGCM values even in the strong-signal and low-variability arena of the equatorial Pacific.

The presence of teleconnections in the AGCM temperatures is shown in Figure 4, with averaged temperature anomalies from the equatorial Pacific (Pac, 80°W–100°E, 20°S–20°N), the equatorial latitudes (Eq, 20°S–20°N), the tropics (Tr, 30°N–30°S), and the northern midlatitudes (30°N–50°N). Magnitudes of the warm midtropospheric response to the 1983 and the 1998 El Niño SSTs diminish and increasingly lag with distance into the northern or southern higher latitudes in both the MSU and the AGCM channel 2 T_b . The chaotic nature of the northern midlatitudes is also displayed, obscuring the El Niño midtropospheric signal.

Similarly, correlations of the AGCM and MSU time series degrade with distance from the equatorial Pacific. As shown in Table 3, midtropospheric temperature correlations over 1979–1998 with only SST forcing are highest in the equatorial latitudes (20°S–20°N) with values above 0.80. Correlations of AGCM and MSU temperature anomalies fall below 0.45 in the northern midlatitudes (30°N–50°N) and below 0.26 in the southern midlatitudes (30°S–50°S). The worst performances occur in the southern high latitudes (50°S–70°S). Similarly, the range of correlations from the SST runs increases with higher latitudes, especially into the Northern Hemisphere. The range in midtropospheric correlations is much more narrow over Northern Hemispheric oceans than over northern landmasses, resembling the low standard deviation seen within tropical latitudes.

The AGCM hindcasts achieve higher Northern Hemispheric correlations over ocean than over land. This performance result is no doubt partly due to the ideal lower boundary condition of observed SSTs. Correlations of the midtroposphere in Table 3 are also consistently higher in the Northern than in the Southern Hemisphere. Within the family of the seven, SST-forced runs, the AGCM Northern Hemispheric correlations remain above 0.51, while the Southern Hemispheric correlations reach only 0.43. Having more landmasses, the Northern Hemisphere has many stationary wave features unlike the Southern Hemisphere, which may explain this strong hemispheric difference in correlations. On the other hand, the northern ocean correlations are consistently higher than the northern land correlations, given the ideal lower boundary of specified SSTs. These Southern Hemispheric correlations should then also benefit from the specified lower boundary. Perhaps the unexpected, weaker southern correlations between AGCM and MSU midtropospheric temperatures are partly due to incorrect reconstructions of Southern Hemispheric SSTs.

The introduction of additional, observed atmospheric forcings does improve the magnitude of the AGCM midtropospheric, warm El Niño responses in global and equatorial Pacific time series (Plate 3). Table 3 lists the corresponding correlations between 3-month-smoothed AGCM and MSU channel 2 temperature anomalies for the 1979–1998 period. The run adding greenhouse gas forcing had correlations significantly lower than the mean correlation from the SST runs, particularly for the equatorial Pacific, the tropical zone, and Northern Hemispheric oceans. Apparently, the greenhouse gas forcing may need to be balanced by other atmospheric forcings in terms of midtropospheric responses. The run adding tropospheric ozone forcing is the only other hindcast to be significantly lower than the SST-run population of correlations for northern oceanic areas. However, the correlation of this run over northern land, where tropospheric ozone forcing occurs (see Fig. A3cd), is comparable to the SST correlations. Also comparison run O3 to run O3s find similar correlations in the northern and low latitudinal zones, making a negative or positive attribution to tropospheric ozone forcing difficult.

Inclusion of stratospheric volcanic aerosols and stratospheric ozone depletion, on the other hand, clearly improve mid-tropospheric temperature hindcasts. The AGCM appears to have spatially re-distributed the forcings' influences. Stratospheric ozone forcing improves correlations significantly relative to the SST runs' population over low latitudes (30°N–30°S) despite stratospheric ozone's stronger changes at polar and high latitudes (see Figure A3a). Likewise, run VOL is signifi-

Table 2. Zonally Averaged AGCM Diagnostics, Control Run Versus Peak El Niños

Diagnostic	Control Ave 10 Januarys	SST f January 1983	SST f January 1998
<i>Subtropical Jet</i>			
Zonal wind, 32°N			
103 mbar	40.3	42.5	45.1 m/s
201 mbar	39.5	41.5	43.7 m/s
<i>Hadley Cell</i>			
Meridional wind, 201 mbar			
8°S	0.78	−0.10	0.06 m/s
8°N	2.46	2.66	2.70 m/s
24°N	0.53	0.28	0.34 m/s
Vertical motion, column average			
6°S	12	10	4 10 ^{−5} mbar/s
2°N	11	33	33 10 ^{−5} mbar/s
10°N	3	−5	−3 10 ^{−5} mbar/s
Stream function, max			
8°S	−62	23	22 10 ⁹ kg/s
0°	−149	−99	−73 10 ⁹ kg/s
8°N	−178	−210	−197 10 ⁹ kg/s
16°N	−144	−150	−140 10 ⁹ kg/s

cantly higher than run GG across northern middle to high latitudes and over northern land despite highest volcanic opacities at low latitudes (see Figure A2). Tropospheric aerosols do not consistently change correlations in the northern latitudinal bins though the run, introducing sulfates, had highest Southern Hemispheric and global correlations. Over southern middle and high latitudes, correlations remain negative or weakly positive regardless of the imposed forcings. While correlations over the northern oceans stay near a maximum of 0.70, the Southern Hemispheric correlations remained low and unresponsive perhaps partly due to the lack of stationary waves, possible flaws in SST reconstructions, and to use of mean sea ice coverage in the AGCM runs.

Globally, best hindcasts of 1979–1998 midtropospheric temperature anomalies have a maximum correlation of 0.66 with MSU observations. Across the equatorial latitudes, AGCM runs achieve correlations close to the maximum of 0.84 if forced by SSTs, greenhouse gases, volcanic opacities, and stratospheric ozone depletion. Results from these single runs exhibit a land-ocean bias: the ocean-dominated Southern Hemispheric correlations were indifferent to imposed atmospheric forcings, while the land-dominated Northern Hemispheric correlations did respond to imposed atmospheric forcings.

3.3. Lower Stratospheric Temperature Time Series

The AGCM lower stratospheric channel 4 T_b values from the seven SST-forced runs, SST a–SST g, appropriately show no volcanic warmings from the 1982 El Chichón and 1991 Mount Pinatubo eruptions. These AGCM channel 4 time series do not exhibit the in situ cooling due to ozone depletions or the presence of quasi-biennial oscillation (QBO) effects. Obviously, the SST record cannot force the AGCM to produce those temporal signatures in its lower stratosphere. Despite simulating cool spatial anomalies during El Niño Januarys over the eastern Pacific (see Plate 2b), correlations of the MSU and

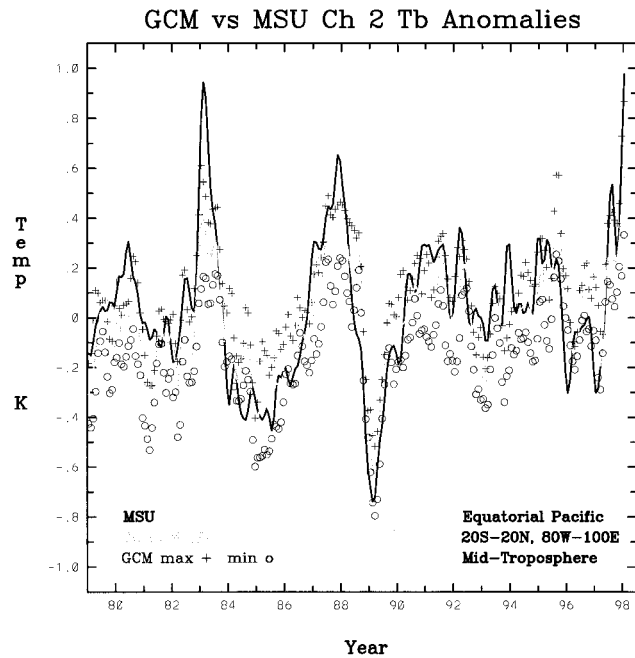


Figure 3. First series of AGCM transient runs forced by observed SSTs does produce El Niño-Southern Oscillation (ENSO) tropospheric warming and cooling responses across the tropics (20°S–20°N). All seven SST-forced AGCM runs are incorporated here in terms of the range of their channel 2 T_b anomalies against the MSU time series. The influence of varying initial conditions, and thus the prompting different internal variability, is nonnegligible. Both time series have smoothing over 3 months to emphasize low-frequency variability.

AGCM channel 4 time series are less than 0.02 in all zones considered, given only SST forcing (Table 4).

Plate 3 shows several AGCM lower stratospheric temperature time series against the MSU time series. The AGCM global lower stratosphere appears to cool slightly over the 1978–1998 period with introduction of the greenhouse gas forcing. Volcanic aerosol opacities on top of this greenhouse gas-cooling force warm events at roughly a third of the MSU-observed El Chichón warming and at almost all of the Mount Pinatubo warming in the 20°S–20°N equatorial zone. The simulation of the El Chichón warming anomaly is slightly improved with inclusion of the stratospheric ozone depletion which cools the AGCM lower stratosphere at a rate similar to that observed by MSU over 1979–1998.

Unlike the troposphere, the AGCM lower stratosphere does equally well in both hemispheres in its correlations with MSU (see Table 4). These correlations also improve substantially with additional atmospheric forcings, and these improvements are coincident with the forcing distribution. Introduction of greenhouse gas forcing raises the Northern Hemispheric correlation by more than 2 standard deviations above the correlations from the SST-forced runs. The low-latitudes, the hemispheric, and the global correlations become significantly different than the SST runs with in situ volcanic aerosol forcing. Stratospheric ozone depletion positively impacts hindcasts, in particular over northern and southern midlatitudes and over southern high latitudes, matching the local distribution of this forcing (see Figure A3a). Tropospheric ozone forcing has a positive impact on northern middle- and high-latitude correlations when added to a background of SST, greenhouse gases,

and volcanic aerosol mixture of forcings, but negative impacts occur on southern high-latitude, hemispheric, and global correlations with the background forcing mixture of SSTs, greenhouse gases, volcanic aerosols, stratospheric ozone, and tropospheric aerosols.

Globally, the AGCM lower stratospheric temperatures correlated up to 0.93 with the MSU time series over the 1979–1998 period, particularly given forcing by greenhouse gases, volcanic aerosols, and stratospheric ozone depletion. Lower stratospheric temperature correlations reached 0.84 levels across the Northern Hemisphere, 0.78 across the Southern Hemisphere, and 0.72 across the tropics.

3.4. Oceanic Lower Tropospheric Temperature Time Series

The AGCM oceanic, lower tropospheric temperature correlations with MSU are not significantly impacted by inclusion of atmospheric forcings on top of SST forcing (see Table 5). The addition of tropospheric carbon and its significant positive impact on the northern high-latitude correlation, from 0.06 to 0.32, is the sole exception. Only oceanic values could be considered due to the lack of observations available to specify AGCM microwave land emissivities with confidence. This MSU channel 2R derives 20% of its full radiance from land surface emission and 10% from ocean surface emission [Shah and Rind, 1995]. Plate 3 shows several of the individual, atmospheric-forcing runs against the observed MSU channel 2R time series. While individual runs do achieve higher channel 2R warming during El Niño events, these higher magnitudes do not change the 1979–1998 correlations of the individual runs significantly in Fisher z -tests. The AGCM lower tropospheric time series correlations also suffer from not reproducing warm anomalies observed prior to mid-1981 in the MSU version c data set.

ENSO variability dominates in these lower tropospheric temperature anomalies. T_b anomaly maps for January 1983 and 1998 in Plate 2c show the strong, Pacific El Niño warmth observed by MSU and hindcast by the AGCM run SST f. The equatorial Pacific (20°S–20°N, 80°W–100°E) and the full equatorial zone (20°S–20°N) thus have the highest correlations between 3-month-smoothed MSU and AGCM time series in Table 5. Many midtropospheric results are sensibly seen again in the lower troposphere: correlations diminish with distance from the tropics; lower tropospheric correlations are consistently better in the Northern than in the Southern Hemisphere; and correlations over the southern middle and high latitudes and the northern high latitudes are low, below 0.40, and occasionally negative.

The performance of the AGCM lower troposphere over oceans is no doubt optimized with the observed SST at its lower boundary. The use of sea ice climatologies, on the other hand, may have limited the lower tropospheric Southern Hemisphere and high-latitude correlations with MSU given higher sensitivity of this channel to surface emission. Nonetheless, the correlations of this channel again cast doubt on Southern Hemispheric SST reconstructions, given the consistently better validations in the Northern Hemisphere.

Globally, the best correlation between oceanic AGCM and MSU channel 2R time series for 1979–1998 was 0.59 from one of the SST-forced runs. Over the equatorial Pacific and across the equatorial zone, lower tropospheric temperature correlations reached maxima of 0.79.

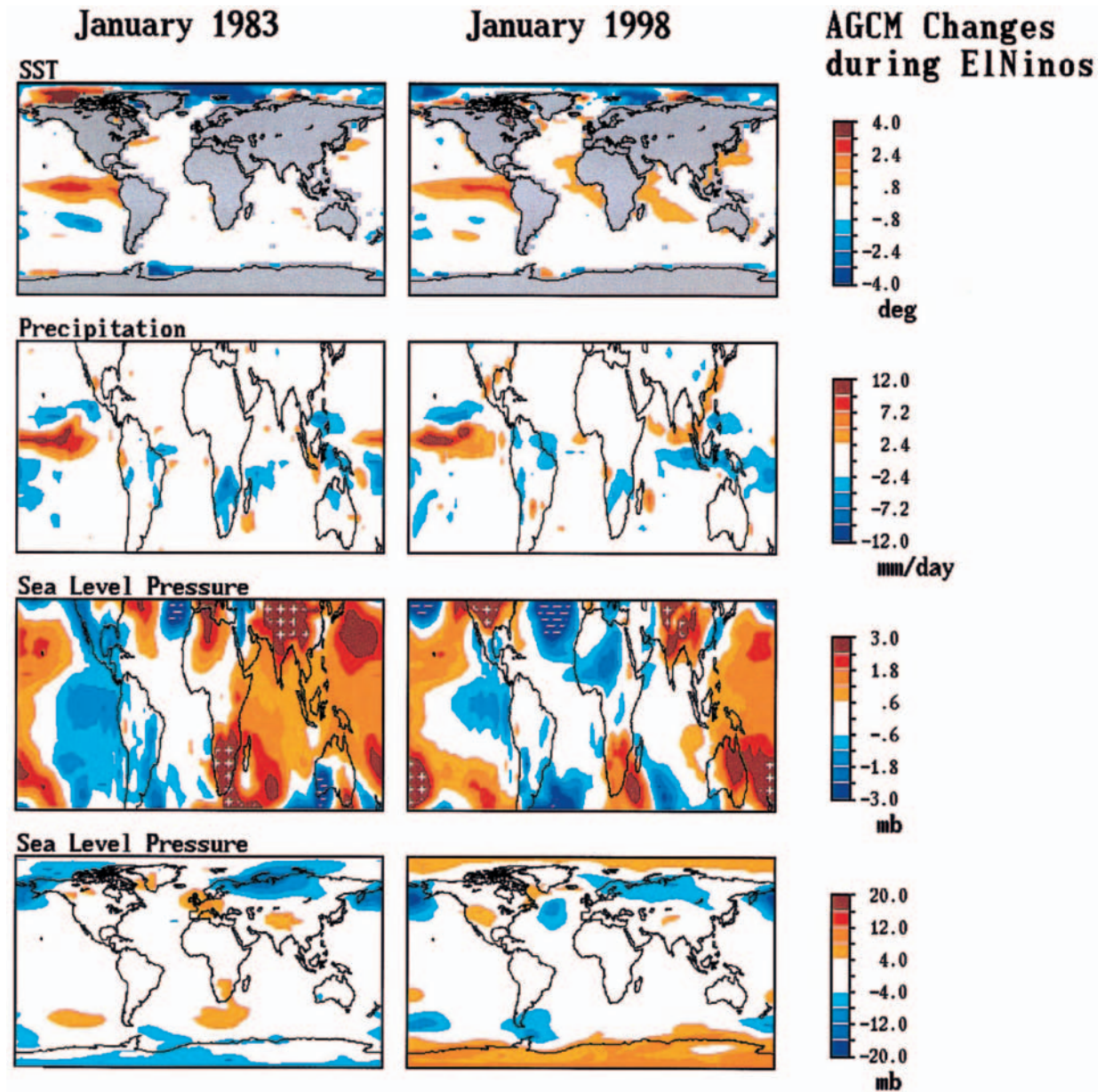


Plate 2a. Differences in AGCM run SST f's sea surface temperatures, precipitation, and sea level pressure are shown for January 1983 and January 1998. Sea level pressure changes are scaled twice to view the large shifts at the Aleutian Low location and the slight shifts over the eastern Pacific.

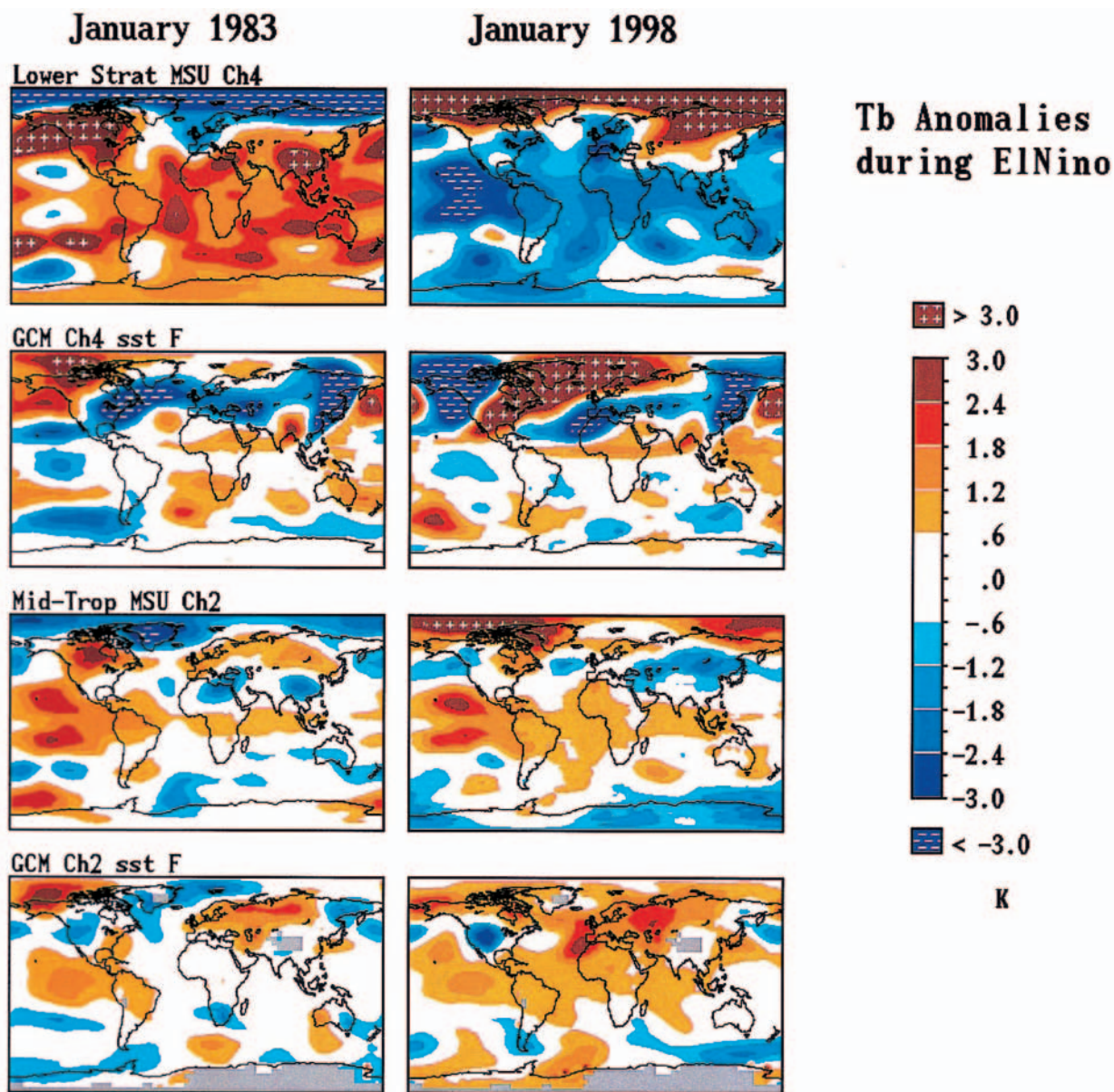


Plate 2b. Regional responses of T_b to El Niño SSTs during January 1983 and January 1998 occur in the lower stratosphere (top rows). Local compensation and cooling in response to movement of the tropopause can be seen in both the MSU and the AGCM T_b . The midtropospheric T_b (middle rows) show the warm “dumbbell” pattern noted by Yulaeva and Wallace [1994] which the AGCM did not consistently generate in discrete centers.

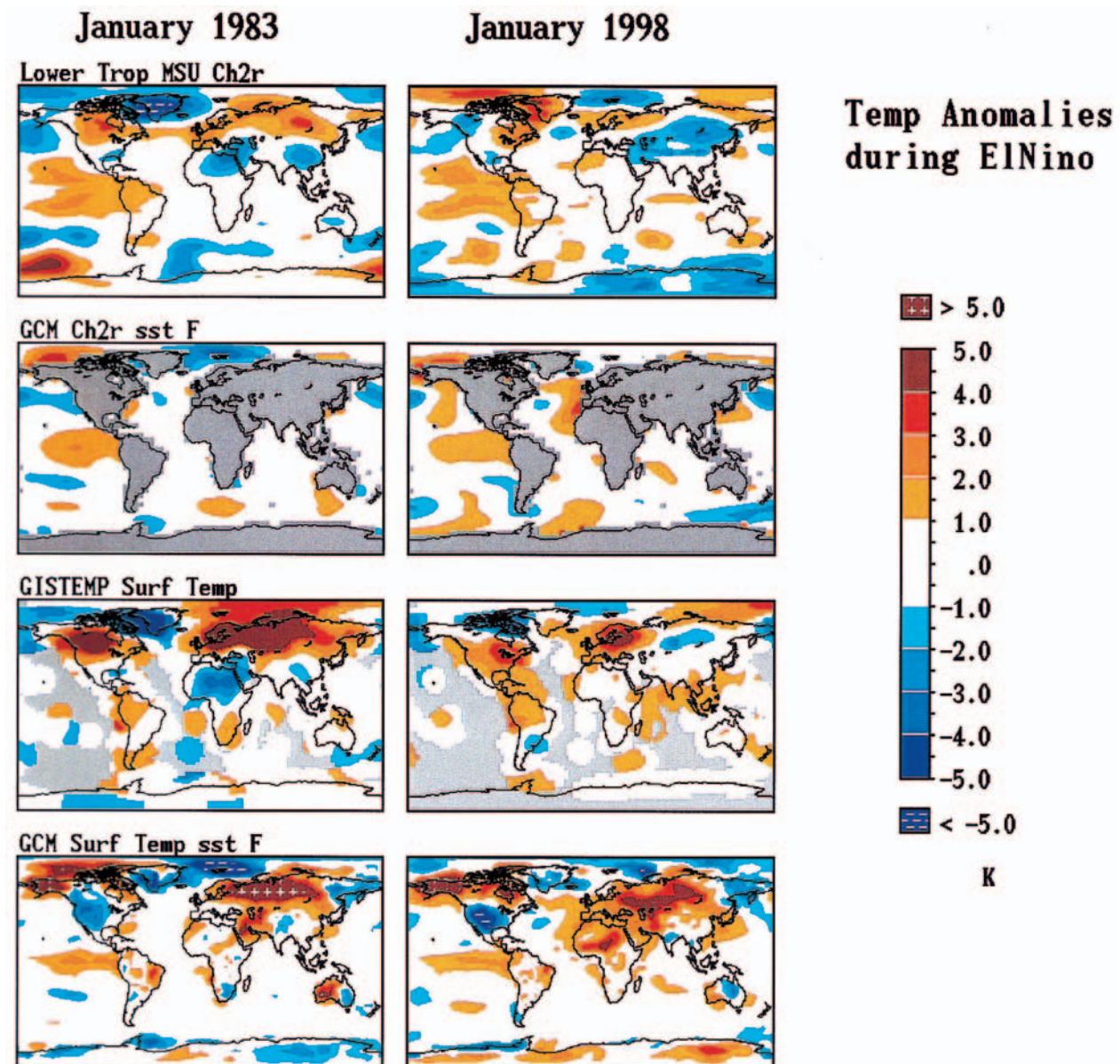


Plate 2c. Lower tropospheric, channel 2R T_b in January 1983 and January 1998 have warm centers over the Pacific akin to midtropospheric T_b anomalies. Observed surface temperature anomalies have patterns similar to those observed for the lower troposphere which are not always hindcast by the AGCM.

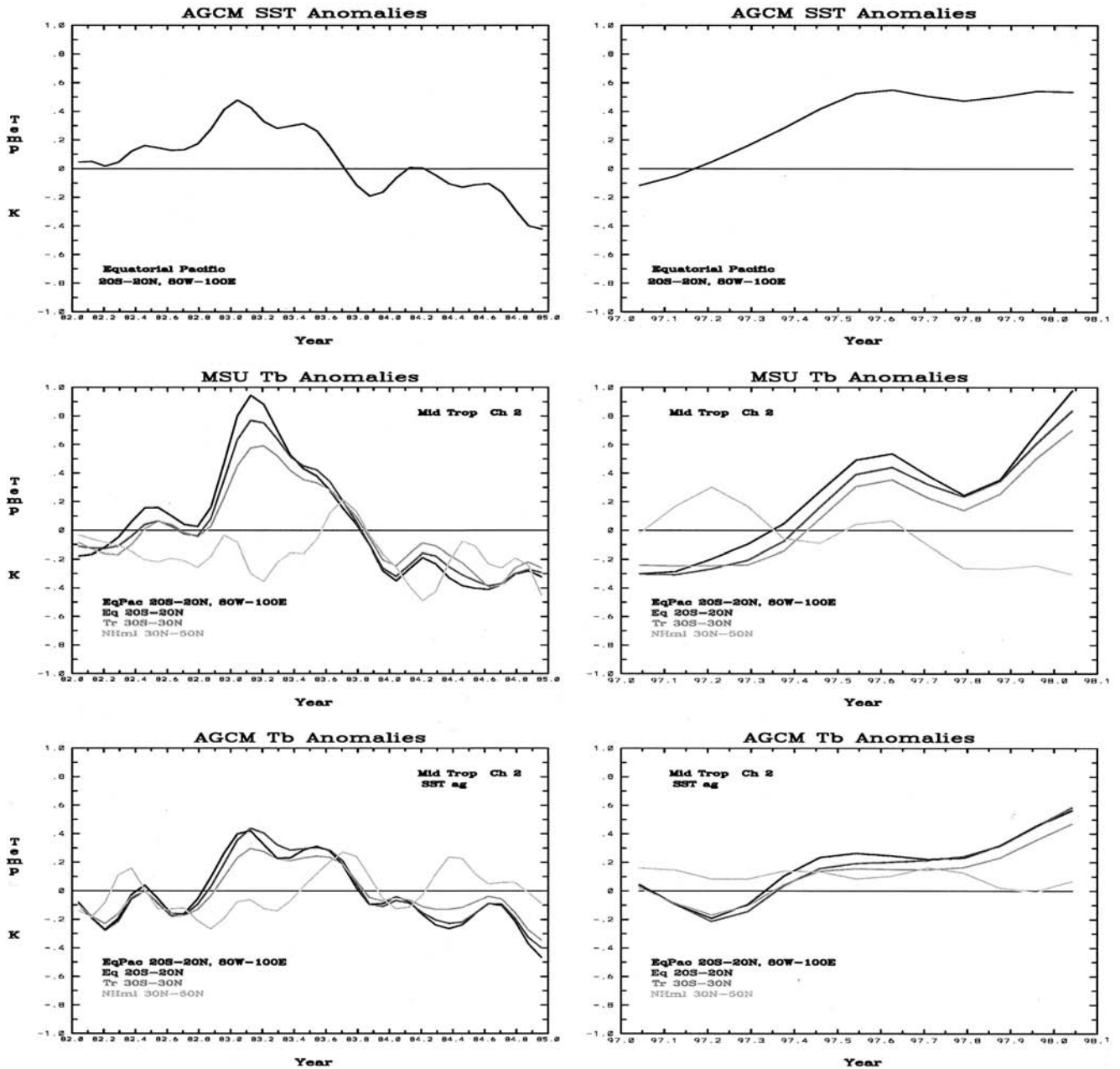


Figure 4. AGCM tropospheric response diminishes in size and has an increasing lag with distance from the tropical Pacific. The warm El Niño response as observed by MSU and as simulated by the AGCM in run SST ag are shown for 1982–1985 (left) and for 1997–1998 (right) as the response moves from the equatorial Pacific into the northern midlatitudes. Smoothing over 3 months has been applied to these time series. See Table 3 for corresponding correlations.

4. Agricultural Region Responses

Three agricultural regions are examined in the following text in terms of their midtropospheric T_b time series, their surface temperature time series, and their precipitation. Nordeste, Zimbabwe, and the U.S. Corn Belt differ in terms of their level of sensitivity and the nature of their responses to ENSO events. These agricultural regions each span only six grid cells in this 4° by 5° AGCM.

Nine out of 11 extreme droughts over northeastern South America from 1911 to 1983 have coincided with El Niño years [Ropelewski and Halbert, 1987]. Nordeste, on Brazil's Atlantic coastline, has lower annual rainfall amounts than most of Bra-

zil and high rainfall only from March to May, given southernmost movement of the Intertropical Convergence Zone (ITCZ). Droughts and famines over Nordeste have caused several large migrations of the population [Chu, 1991]. Drayan *et al.* [2000] detailed the enhanced subsidence of El Niño years, warmer surface air temperatures, and drought events over Nordeste in compensation for the anomalously strong convection over the Pacific coast of South America. However, tropical Atlantic SST anomalies correlated even more strongly with Nordeste precipitation. The ITCZ follows the latitude of the warmest SST. Thus warm SSTs in the tropical North Atlantic tend to cause less of a southward migration of the ITCZ. The

Table 3. Correlations of AGCM and MSU 3-Month-Smoothed Ch 2 Trop T_b Time Series, 1979–1998

Run	Pac 20°S–20°N 80°W–100°E	Eq 20°S–20°N	Tr 30°S–30°N	NH mid 30°–50°N	NH hi 50°–70°N	NH la	NH oc	SH mid 30°S–50°S	SH hi 50°–70°S	SH	NH	G
<i>SST Forcing</i>												
SST a	0.79	0.83	0.77	0.29	0.30	0.39	0.69	0.26	−0.12	0.40	0.57	0.63
SST b	0.75	0.79	0.74	0.33	0.26	0.47	0.69	0.16	0.01	0.26	0.61	0.58
SST c	0.77	0.81	0.73	0.32	0.22	0.36	0.68	0.26	0.06	0.35	0.55	0.52
SST d	0.72	0.80	0.75	0.45	0.19	0.48	0.69	0.19	−0.15	0.31	0.64	0.57
SST e	0.75	0.76	0.71	0.43	0.29	0.48	0.69	0.25	−0.10	0.38	0.62	0.57
SST f	0.77	0.81	0.77	0.40	−0.06	0.36	0.67	0.26	0.07	0.43	0.57	0.60
SST g	0.76	0.79	0.75	0.20	0.04	0.30	0.64	0.17	−0.10	0.42	0.51	0.55
SST mean	0.76	0.80	0.75	0.35	0.18	0.41	0.68	0.22	−0.05	0.36	0.58	0.57
SST std	0.02	0.02	0.02	0.09	0.14	0.07	0.02	0.05	0.09	0.06	0.04	0.03
<i>SST Ensemble</i>												
SST ag	0.81	0.86	0.82	0.50	0.27	0.55	0.76	0.29	−0.10	0.46	0.70	0.66
<i>Atmospheric Forcing</i>												
GG	(0.71)	0.76	(0.70)	0.33	0.12	0.30	(0.60)	0.13	0.00	0.34	(0.48)	(0.49)
VOL	0.74	0.76	0.72	[0.50]	[0.31]	[0.54]	0.66	0.21	0.05	0.40	[0.62]	0.58
O3s	([0.82])	[0.84]	([0.80])	0.35	0.18	0.44	0.68	0.18	−0.03	(0.50)	0.58	0.60
O3t	0.79	0.81	0.74	0.39	0.20	[0.40]	(0.60)	0.14	−0.01	0.35	[0.51]	0.51
O3	([0.82])	[0.83]	([0.80])	0.42	0.33	0.52	0.70	([0.03])	[−0.15]	0.39	0.65	0.62
O3sS	0.79	0.83	0.79	0.25	[0.39]	0.50	0.67	0.19	0.10	(0.50)	0.62	(0.66)
O3sSC	0.78	0.80	0.74	[0.50]	0.36	0.51	0.70	0.11	[−0.06]	[0.33]	0.63	0.59
O3SC	0.77	0.78	0.72	0.40	0.30	0.46	0.66	0.11	−0.04	0.26	0.57	(0.50)

Pac, Pacific; Eq, equatorial; Tr, tropical; NH mid, Northern Hemisphere midlatitudes; SH hi, Southern Hemisphere high latitudes; la, land; oc, ocean; G, global; mean, average of seven SST correlations; and std, standard deviation of seven SST correlations. Correlations in parentheses are more than 2 standard deviations away from the SST run mean correlation. Correlations in brackets differ significantly from a previous run correlation based on a Fisher z -test. Run GG is compared to the mean SST; run VOL to GG; runs O3s, O3t, and O3 to VOL; run O3sS to O3s; run O3sSC to O3sS; and, run O3SC to O3sSC.

reverse is true: cool SSTs north of the equator and warm SSTs south of the equator in the Atlantic promote further southward placement of the ITCZ and wetter years over Nordeste.

Matarira [1990] found that Zimbabwe similarly suffers rainfall deficits during El Niño years. *Cane et al.* [1994] extended these relationships with strong correlations between NINO3 SSTs and maize yield in Zimbabwe. Normally Zimbabwe receives 80–90% of its precipitation from November to March due to the presence of the ITCZ over the area. The country's topography features high mountains along its eastern border with Mozambique, topography much higher than the other two agricultural regions considered herein. During El Niño years there appears to be a northeastward shift of rainfall towards the island of Madagascar and the Indian Ocean related to the shift of convection areas in the tropical belt [*Matarira*, 1990; *Druryan et al.*, 2000]. As seen with Nordeste, however, interannual variability of Zimbabwe's climate is only partly shaped by ENSO events, being also affected by land surface conditions, SSTs of the Atlantic and Indian oceans, and other local sources of atmospheric variability.

Phillips et al. [1999] examined relationships between ENSO SST anomalies and the maize yields from the USDA/NASS Crops Count Data and the monthly observed precipitation and surface temperature from NOAA. They determined that roughly 15% of the interannual maize yield variability in the U.S. Corn Belt was due to ENSO forcing. The positive impact of cooler temperatures and enhanced rainfall during El Niño years was less influential than the detrimental warmer and drier summers of La Niña years.

4.1. Midtropospheric Temperatures

The MSU time series in Figure 4 clearly show ENSO signals in the midtroposphere becoming noise-obscured and delayed

with entrance into the northern midlatitude band. The observed midtropospheric temperature time series over the U.S. Corn Belt is similarly extremely noisy and lacks any distinct signals despite experiencing some cooler temperature anomalies during the 1983 and 1987 El Niño years (see Figure 5). Both Nordeste and Zimbabwe, on the other hand, experience the expected warmer midtropospheric temperature signals concurrent with ENSO SSTs. AGCM hindcasts of these two tropical agricultural regions show similar warm events and agree with MSU time series in being more lucid and coherent over Nordeste than over Zimbabwe (Plate 4).

Table 6a lists the corresponding MSU and AGCM correlations for the 1979–1998 period over the three regions. The Nordeste hindcasts correlate as high as 0.80, while Zimbabwe reaches only 0.54, and the U.S. Corn Belt, lacking any strong midtropospheric temperature signal in its time series, has values below 0.25. Zimbabwe's weak performance may be partly due to its extreme topography and subsequent local synoptic patterns which may not be constrained by the 4° by 5° AGCM. Hindcast of the full 30°S–30°N tropical belt, as discussed earlier, showed more sensitivity to additional atmospheric forcings than these agricultural regions. Correlations of the Nordeste monthly midtropospheric temperatures remain within the range of correlations given by the SST runs regardless of introduced atmospheric forcings. Zimbabwe saw the only significant improvement relative to the SST series with the greenhouse gases run, moving to a correlation 0.54 from a mean SST value of 0.34. This is opposite the response by the full tropical midtroposphere, which suffered negative impacts when only greenhouse gas forcing was added and not balanced by other forcings, as discussed earlier.

The AGCM has varying seasonal performance over Nordeste and Zimbabwe as detailed in Table 6b. The AGCM

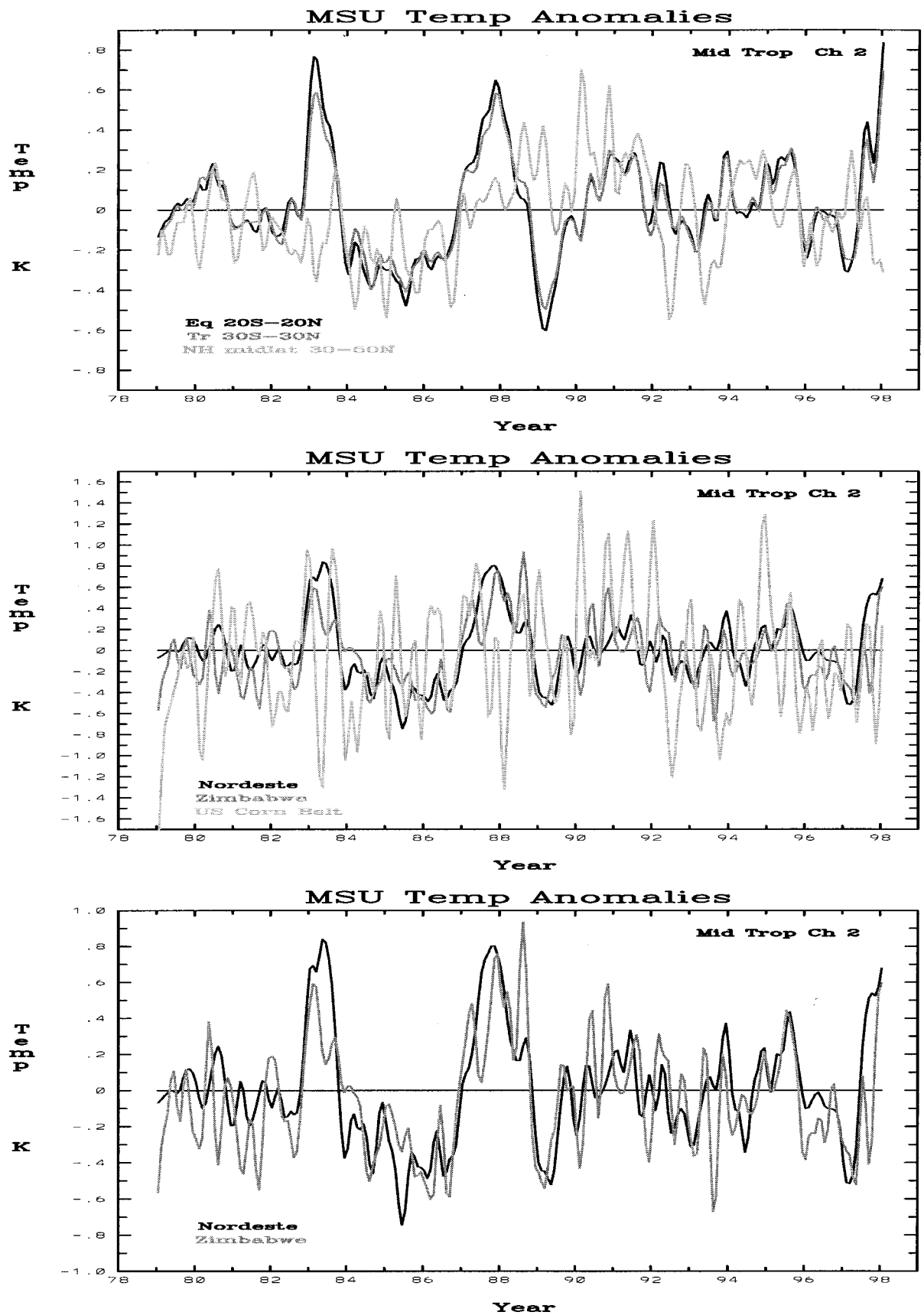


Figure 5. ENSO signal in the MSU midtropospheric channel 2 anomalies becomes obscured by other sources of variability outside of the tropical (30°S–30°N) latitudes (top). Consequently, while Nordeste in northeastern Brazil and Zimbabwe have clear ENSO signals in their midtropospheric temperatures (bottom), the U.S. Corn Belt has a noisy midtropospheric temperature time series (middle). Note that the temperature scale increases to accommodate U.S. Corn Belt variability. Smoothing over 3 months has been applied to these time series. Correlations for these time series are in Tables 6a and 6b.

Table 4. Correlations of AGCM and MSU 3-Month-Smoothed Ch 4 Lower Strat T_b Time Series, 1979–1998

Run	Pac 20°S–20°N 80°W–100°E	Eq 20°S–20°N	Tr 30°S–30°N	NH mid 30°–50°N	NH hi 50°–70°N	SH mid 30°–50°S	SH hi 50°–70°S	SH	NH	G
<i>SST Forcing</i>										
SST mean	−0.01	−0.01	0.03	−0.05	0.12	0.10	0.08	0.06	0.01	0.00
SST std	0.09	0.11	0.11	0.11	0.06	0.05	0.08	0.11	0.13	0.21
<i>SST Ensemble</i>										
SST ag	−0.03	−0.02	0.03	−0.09	0.20	0.17	0.17	0.08	0.03	0.01
<i>Atmospheric Forcing</i>										
GG	0.07	0.15	0.17	−0.17	0.18	0.09	0.01	0.09	([0.31])	[0.32]
VOL	([0.48])	([0.52])	([0.60])	([0.12])	0.04	([0.51])	0.12	([0.71])	([0.59])	([0.81])
O3s	([0.60])	(0.62)	(0.68)	([0.48])	([0.26])	(0.60)	([0.31])	(0.75)	([0.83])	([0.90])
O3t	(0.51)	(0.51)	(0.58)	([0.49])	([0.31])	(0.55)	(0.01)	([0.61])	(0.67)	(0.79)
O3	(0.55)	(0.56)	(0.66)	(0.24)	([0.26])	(0.38)	(0.20)	(0.73)	(0.62)	(0.82)
O3sS	(0.59)	(0.63)	(0.70)	(0.50)	(0.14)	(0.59)	(0.29)	(0.76)	(0.83)	(0.91)
O3sSC	(0.63)	(0.66)	(0.72)	(0.38)	(0.26)	(0.53)	(0.44)	(0.78)	(0.84)	(0.93)
O3SC	(0.55)	(0.58)	(0.63)	(0.41)	(0.25)	(0.41)	([0.06])	([0.68])	([0.68])	([0.82])

midtroposphere over Nordeste matches MSU time series best in the winter (JJA) and spring (SON) and exhibits narrower ranges for the distribution of correlations from the SST runs. In a few instances the Nordeste spring (SON) and summer (DJF) in runs with additional atmospheric forcings fall outside the distribution of correlations from the SST-forced runs. Its fall (MAM) performance, when northeastern Brazil receives most of its rain, is moderately good but exhibits the widest range in correlations. The AGCM shows variability to its positioning the ITCZ southernmost migration and the subsidence balancing eastern Pacific convection during El Niños despite usage of observed Atlantic and Pacific SSTs. This argues for usage of an average of several runs to hindcast Nordeste midtropospheric temperatures despite inherent dilution of extreme events.

AGCM midtropospheric hindcasts over Zimbabwe do similarly in every season except winter (JJA), which has several negative correlations with MSU and a large standard deviation around the mean correlation of the SST runs. Lower correla-

tions with observations during the Southern Hemisphere winter may be partly due to the AGCM higher-than-observed interannual variability during that season (see Figure 2). Zimbabwe receives most of its rainfall from November to March due to the ITCZ presence, and overlapping seasons in the AGCM hindcasts have higher correlations and lower standard deviations. This seasonality to midtropospheric performance by the AGCM is preferable.

Like Nordeste, several midtropospheric time series for Zimbabwe during spring (SON) and summer (DJF) lie outside the distribution of correlations from the SST runs. Unlike Nordeste, these time series also differ significantly in Fisher z -tests from other individual runs if only in one season. As suggested by the monthly correlations of Table 6a, the run adding greenhouse gases sees almost year-round improvement over Zimbabwe, significantly raising the winter (JJA) correlation relative to the mean SST correlation, 0.34 relative to 0.00, and improving the fall and spring correlations.

Table 5. Correlations of AGCM and MSU 3-Month-Smoothed Oceanic Ch 2R Lower Trop T_b Time Series, 1979–1998

Run	Pac 20°S–20°N 80°W–100°E	Eq 20°S–20°N	Tr 30°S–30°N	NH mid 30°–50°N	NH hi 50°–70°N	SH mid 30°–50°S	SH hi 50°–70°S	SH	NH	G
<i>SST Forcing</i>										
SST a	0.79	0.79	0.71	0.57	0.22	0.37	−0.04	0.40	0.55	0.57
SST b	0.76	0.70	0.71	0.51	0.25	0.18	−0.04	0.17	0.66	0.49
SST c	0.77	0.77	0.68	0.53	0.09	0.40	0.07	0.35	0.61	0.52
SST d	0.73	0.74	0.67	0.51	0.29	0.38	−0.08	0.26	0.62	0.48
SST e	0.77	0.74	0.67	0.59	0.15	0.30	0.04	0.31	0.63	0.53
SST f	0.76	0.75	0.70	0.58	0.22	0.24	0.10	0.40	0.66	0.59
SST g	0.77	0.78	0.73	0.54	0.36	0.23	−0.09	0.33	0.64	0.56
SST mean	0.76	0.76	0.70	0.55	0.22	0.30	−0.01	0.32	0.62	0.53
SST std	0.02	0.02	0.02	0.03	0.09	0.08	0.07	0.08	0.04	0.04
<i>SST Ensemble</i>										
SST ag	0.80	0.80	0.73	0.68	0.41	0.38	−0.01	0.37	0.72	0.60
<i>Atmospheric Forcing</i>										
GG	0.72	0.72	(0.63)	0.52	0.24	0.26	0.07	0.23	0.61	0.46
VOL	0.77	0.74	0.67	0.60	0.28	0.26	0.05	0.33	0.65	0.54
O3s	0.80	0.78	0.72	0.56	0.25	0.24	−0.02	0.36	0.62	0.54
O3t	0.78	0.77	0.67	0.57	(0.03)	0.32	(0.14)	0.25	0.57	0.45
O3	0.79	0.77	0.71	(0.62)	0.12	(0.12)	(−0.21)	0.22	0.62	0.49
O3sS	0.76	0.77	0.70	0.52	0.06	0.33	0.06	0.40	0.64	0.56
O3sSC	0.73	0.70	(0.61)	0.59	[0.32]	0.16	0.01	0.25	0.63	0.47
O3SC	0.78	0.76	0.67	0.57	0.24	0.29	−0.03	0.26	0.67	0.52

Overall, Nordeste midtropospheric temperature hindcasts do not change significantly with the addition of other known forcings over the 1979–1998 period. Winter and spring midtropospheric temperatures over Nordeste achieve the highest correlation of 0.76 and 0.74, respectively, with MSU data. Midtropospheric hindcasts over Zimbabwe change significantly with the addition of several atmospheric forcings but only in one season and with mixed influence on the other seasons. The best 1979–1998, full time series correlation over Zimbabwe of 0.54 from run GG comes from significant improvement in the winter temperature anomalies and some improvement in the spring and fall temperature anomalies.

4.2. Surface Temperatures

The GISTEMP surface temperature observations in Figure 6 show ENSO signals which become hidden by other sources of variability as the scale diminishes from global to North Hemispheric to Northern Hemispheric land averaging. Also, these surface temperature time series clearly show a warming trend, particularly over Northern Hemispheric land (J. Hansen et al., 1999). The surface air temperature record, like the midtroposphere, over the U.S. Corn Belt is extremely noisy, while warm El Niño signals in the 1980s occur over Nordeste at 1.3° and over Zimbabwe at 1.5°.

Figure 7 shows the GISTEMP and AGCM surface air temperature time series over Northern Hemispheric land and the two tropical agricultural regions. The AGCM time series is the average of the seven SST-forced runs, SST ag. As with the midtropospheric temperatures, the AGCM surface air temperature hindcast is more coherent over Nordeste than Zimbabwe. This average of the seven SST-forced runs does not generate the surface air temperature warming seen in the observations over Northern Hemisphere (NH) land.

Table 7a again shows that though additional atmospheric forcings often improve AGCM performance over latitudinal zones, these forcings do not necessarily prompt changes over small agricultural areas. The range in SST run correlations of

Table 6a. Regional Correlations of AGCM and MSU 3-Month-Smoothed Ch 2 Trop T_b Time Series, 1979–1998

Run	Nordeste 4°S–12°S 37°W–48°W	Zimbabwe 16°S–24°S 22.5°E–32.5°E	U.S. Corn Belt 36°N–44°N 87.5°W–97.5°W
<i>SST Forcing</i>			
SST a	0.73	0.39	0.11
SST b	0.74	0.42	0.12
SST c	0.80	0.24	−0.04
SST d	0.73	0.39	0.15
SST e	0.73	0.19	0.14
SST f	0.68	0.42	0.21
SST g	0.71	0.34	0.01
SST mean	0.73	0.34	0.10
SST std	0.03	0.09	0.09
<i>SST Ensemble</i>			
SST ag	0.81	0.59	0.16
<i>Atmospheric Forcing</i>			
GG	0.73	([0.54])	−0.05
VOL	0.70	[0.39]	0.08
O3s	0.72	0.27	0.08
O3t	0.74	0.40	0.00
O3	0.75	0.26	0.17
O3sS	0.74	0.40	0.25
O3sSC	0.73	0.37	[0.03]
O3SC	0.73	[0.16]	0.01

Table 6b. Regional Correlations of AGCM and MSU Ch 2 Trop T_b Time Series, Seasons 1979–1998

Run	Nordeste 4°S–12°S 37°W–48°W				Zimbabwe 16°S–24°S 22.5°E–32.5°E			
	DJF	MAM	JJA	SON	DJF	MAM	JJA	SON
<i>SST Forcing</i>								
SST a	0.49	0.59	0.63	0.64	0.21	0.08	0.04	0.31
SST b	0.57	0.50	0.68	0.68	0.02	0.25	0.26	0.29
SST c	0.60	0.74	0.75	0.68	0.28	0.10	−0.20	0.36
SST d	0.58	0.57	0.67	0.68	0.23	0.30	0.25	0.19
SST e	0.57	0.57	0.70	0.64	0.22	0.11	−0.15	0.12
SST f	0.40	0.52	0.64	0.61	0.22	0.20	0.16	0.34
SST g	0.51	0.48	0.69	0.66	0.08	0.37	−0.11	0.37
SST mean	0.53	0.57	0.68	0.66	0.18	0.20	0.00	0.28
<i>SST Ensemble</i>								
SST std	0.07	0.09	0.04	0.03	0.09	0.11	0.19	0.10
SST ag	0.65	0.65	0.80	0.81	0.34	0.46	0.01	0.52
<i>Atmospheric Forcing</i>								
GG	0.40	0.60	0.69	0.71	0.16	0.38	[0.34]	0.46
VOL	0.50	0.53	0.76	(0.59)	0.10	0.21	0.27	0.31
O3s	0.43	0.65	0.66	0.61	0.10	0.34	0.17	[(0.05)]
O3t	0.52	0.56	0.68	0.68	[(0.37)]	0.37	0.27	0.19
O3	0.49	0.57	0.69	0.71	0.14	0.24	0.12	0.17
O3sS	0.46	0.66	0.71	0.65	[(0.54)]	0.32	0.21	0.10
O3sSC	(0.36)	0.66	0.76	(0.74)	[0.22]	0.14	−0.03	0.25
O3SC	0.40	0.57	0.74	0.68	0.23	0.14	−0.12	0.06

surface temperatures resembles that found for the AGCM midtropospheric temperatures (see Tables 3 and 6a). While the agricultural region performances are generally lower than seen for the midtroposphere, surface temperature correlations over northern landmasses are comparable or better than midtropospheric correlations. The Northern Hemispheric land correlations of surface temperature show significant improvement relative to the SST-forced distribution of correlations. More atmospheric-forcing runs have a northern land correlation 2 standard deviations higher than the mean SST-forced correlation for surface temperature than for midtropospheric temperature. AGCM hindcasts of surface temperatures over Nordeste, however, remain close to the maximum correlation of 0.46 and indifferent to introduced atmospheric forcings. Correlations for Zimbabwe and the U.S. Corn Belt are mostly below 0.20 and sometimes negative.

Examination of the 1979–1995, unsmoothed seasonal time series finds no improvement to the U.S. Corn Belt or Zimbabwe surface air temperature correlations. Nordeste and northern land seasonal correlations in Table 7b exhibit strong seasonal dependence and reach higher correlations than seen from the monthly, smoothed time series. The AGCM surface air temperatures over both Nordeste and the Northern Hemispheric land do well during the JJA season, reaching 0.64 and 0.62 correlations, respectively. Nordeste also sees consistently stronger surface temperature correlations during its fall (MAM) season. Since Nordeste suffers from anomalous SST impacts on its peak precipitation during the fall season, this seasonal performance by the AGCM is optimal.

The northern landmasses have best surface temperature correlations during northern summer (JJA) and fall (SON) seasons. The summer season shows high responsiveness to additional atmospheric forcings, performing particularly well in run VOL and the run adding in soot, run O3sSC despite higher standard deviation in correlations in the SST runs. Crop pro-

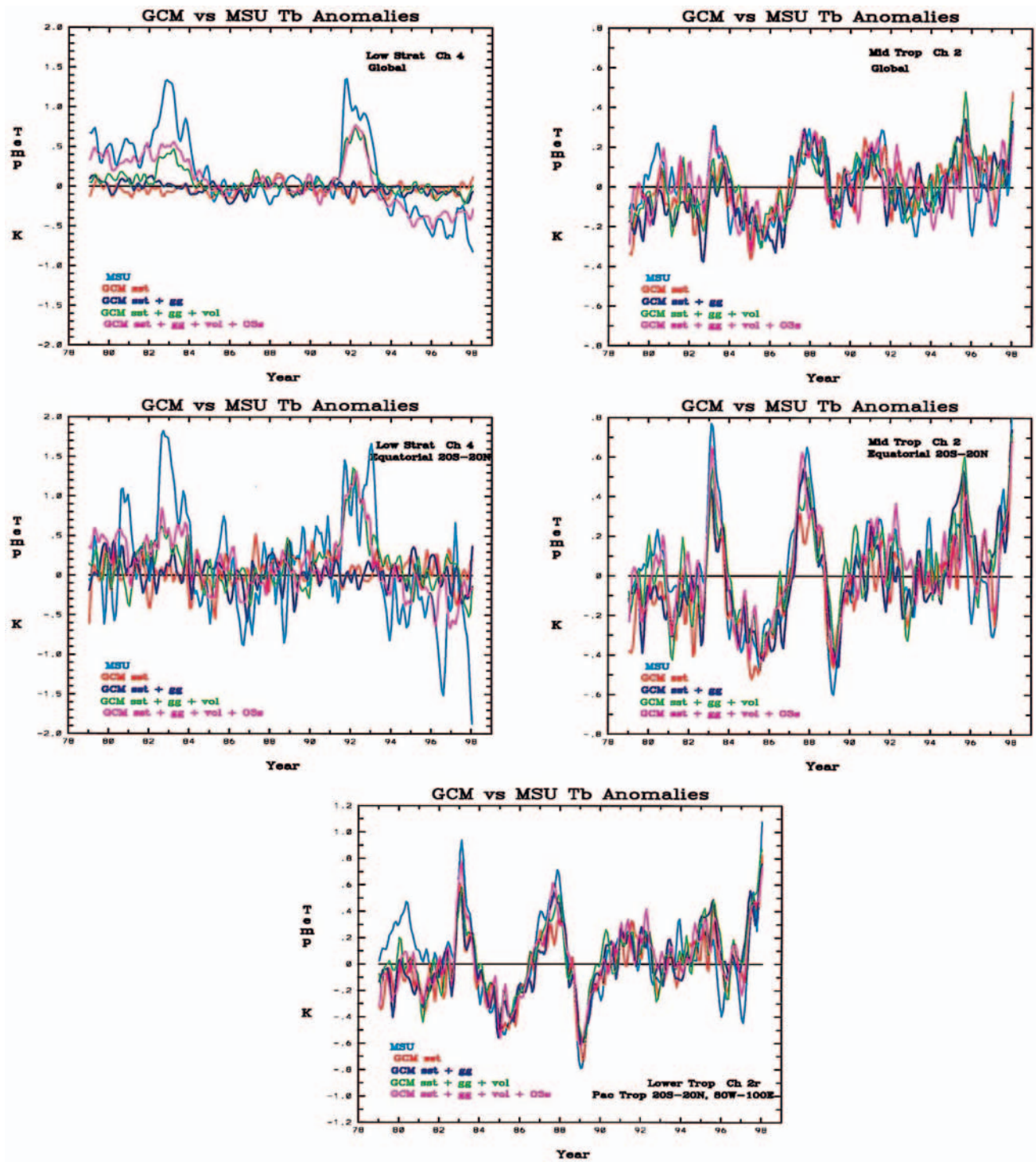


Plate 3. Agreement between the AGCM lower stratospheric (left), midtropospheric (right) and oceanic lower tropospheric (bottom) time series and MSU time series improves during El Niño events with inclusion of known atmospheric forcings. Disagreement between the AGCM and MSU oceanic lower tropospheric time series remain notable prior to mid-1981. Smoothing over 3 months has been applied to these time series. See Tables 3, 4, and 5 for corresponding correlations.

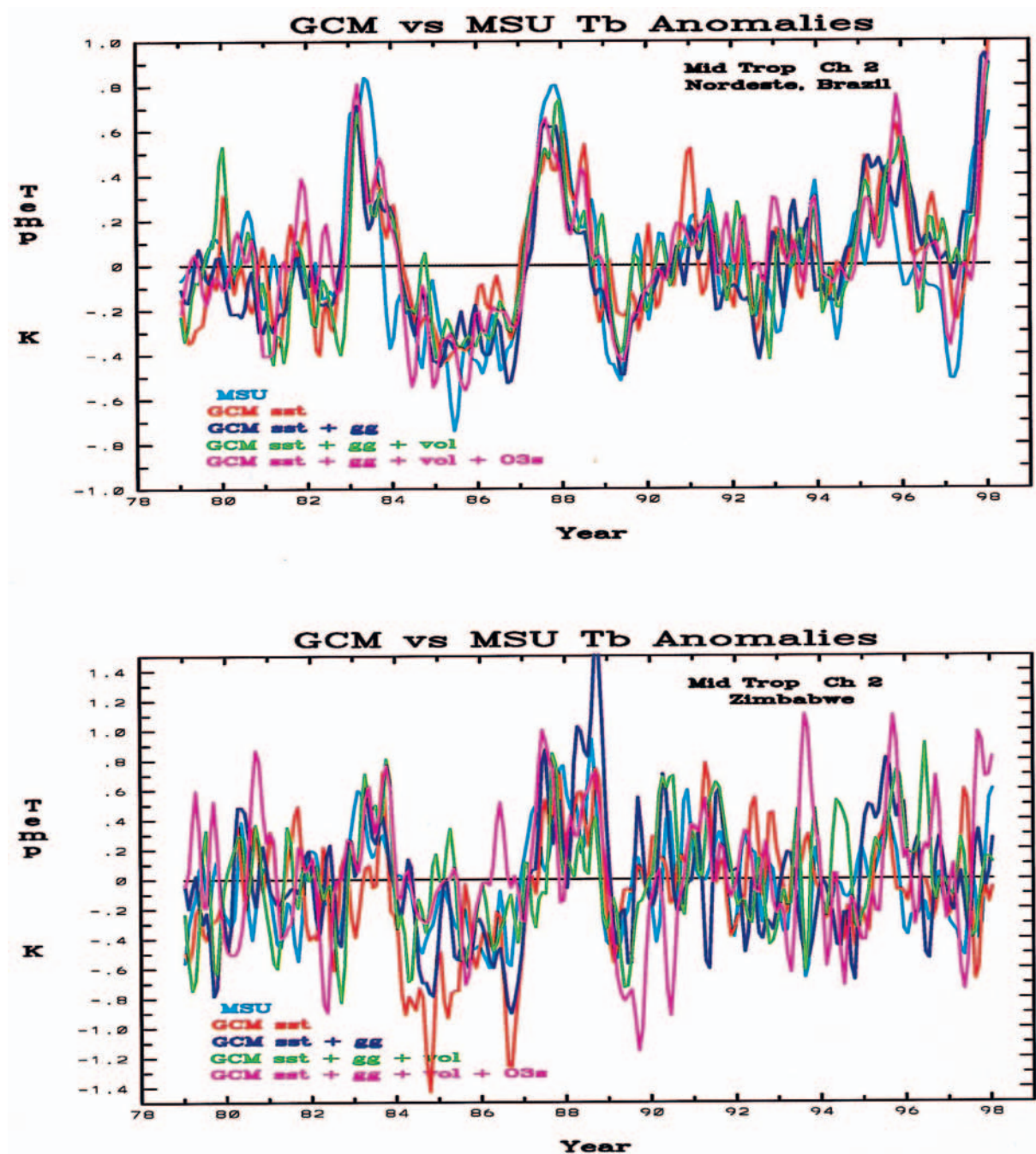


Plate 4. Agreement between the AGCM midtropospheric temperature time series and MSU observations over Nordeste and Zimbabwe did not change notably with inclusion of known atmospheric forcings though stronger ENSO responses occur. Smoothing over 3 months has been applied to these time series. Correlations for these time series are in Tables 6a and 6b.

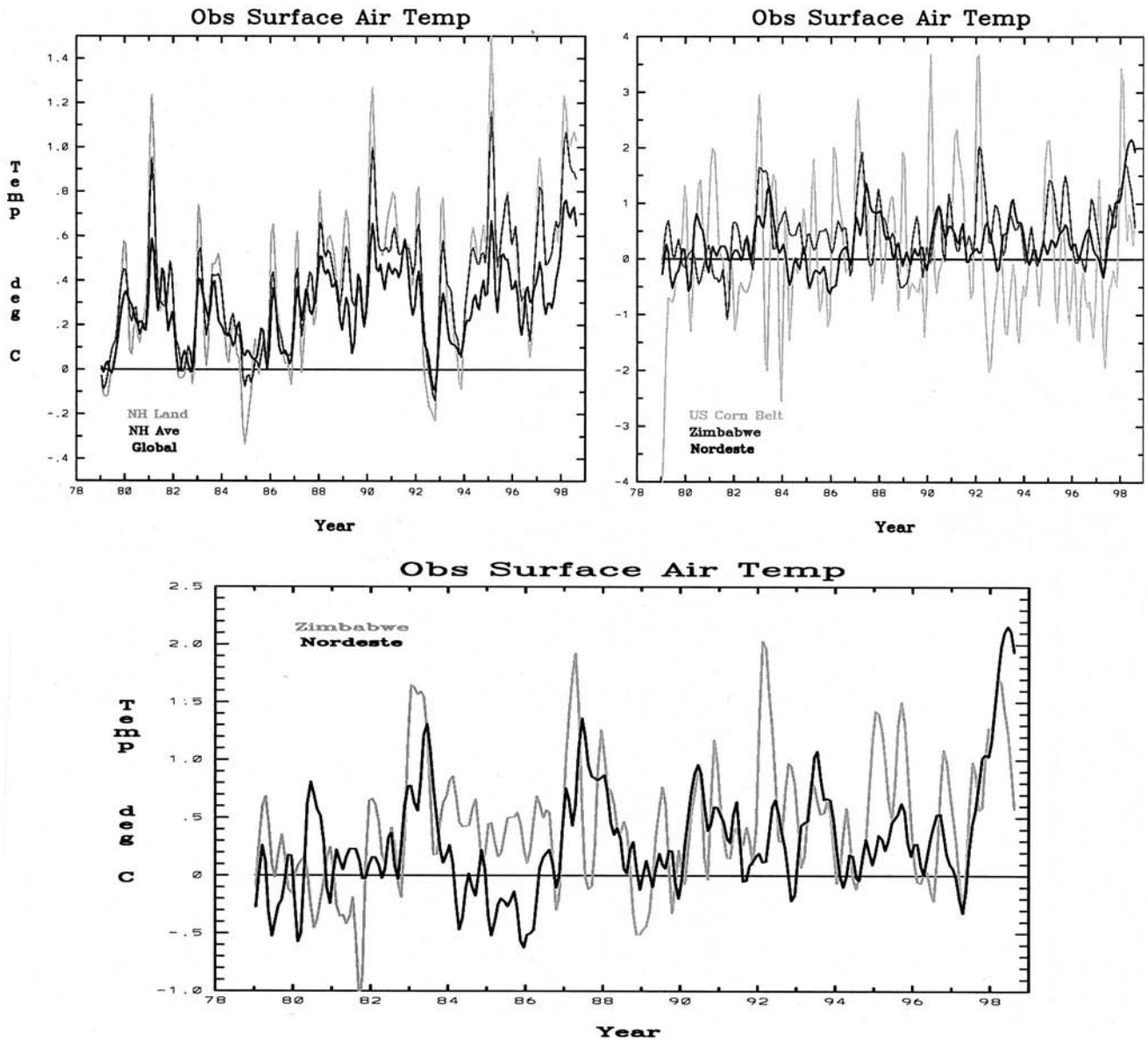


Figure 6. Meteorological station surface temperatures from the GISTEMP data set [Hansen et al., 1999] are shown in global, Northern Hemisphere, and Northern Hemisphere land averages to emphasize the increased variability over land (top left). These surface temperatures clearly show a warming trend. The ENSO signal, as seen for the midtroposphere, becomes obscured by other sources of variability outside of the equatorial (30°S–30°N) latitudes. Consequently, while Nordeste in northeastern Brazil and Zimbabwe have clear ENSO signals in their surface temperatures (bottom), the U.S. Corn Belt has a noisy surface temperature time series (top right). Smoothing over 3 months has been applied to these time series.

duction over the United States relies on germination and establishment during the spring (MAM) months and tasseling and grain fill during the summer months (JJA), so the good summer performance is encouraging, but the performance of the AGCM could be improved.

4.3. Precipitation

AGCM precipitation anomalies in the agricultural regions are validated against rain gage observations over 1979–1997 from Hastenrath and Greischar [1993], the Zimbabwe Meteorological Service, and NOAA/NCDC. As in the case of tropospheric and surface temperatures, AGCM precipitation anomalies for Nordeste exhibit interannual responses that parallel

observations. The average of the seven atmospheres simulated with SST forcing, SST ag, achieves a 0.59 correlation with observations with 5-month smoothing applied to both AGCM and observational time series and only a 0.45 correlation with unsmoothed time series. The highest precipitation correlation of 0.63 occurs with one of the individual SST runs, SST c (see Table 8).

Correlations between observed and hindcast time series of Nordeste precipitation are comparable with or without the additional atmospheric forcings in Table 8. Inclusion of forcing from tropospheric ozone may have worsened precipitation hindcasts as correlations from the runs, including this forcing (correlations 0.49, 0.43 and 0.48), all fall below correlations

Table 7a. Regional Correlations of AGCM and GISTEMP 3-Month-Smoothed Surface Air Temperature Time Series, 1979–1995

Run	Nordeste 4°S–12°S 37°W–48°W	Zimbabwe 16°S–24°S 22.5°E–32.5°E	U.S. Corn Belt 36°N–44°N 87.5°W–97.5°W	NH Land
<i>SST Forcing</i>				
SST a	0.45	0.10	0.13	0.36
SST b	0.35	0.24	−0.06	0.48
SST c	0.39	0.09	−0.06	0.47
SST d	0.41	0.17	0.05	0.40
SST e	0.41	0.11	0.12	0.39
SST f	0.36	−0.03	0.09	0.28
SST g	0.46	0.31	0.01	0.41
SST mean	0.41	0.14	0.04	0.40
SST std	0.04	0.09	0.08	0.05
<i>SST Ensemble</i>				
SST ag	0.49	0.31	0.07	0.55
<i>Atmospheric Forcing</i>				
GG	0.42	−0.05	−0.04	0.32
VOL	0.38	0.00	0.08	([0.55])
O3s	0.38	([0.37])	0.08	0.50
O3t	0.33	0.18	(−0.14)	(0.62)
O3	0.39	0.00	0.04	(0.60)
O3sS	0.46	0.10	0.12	(0.51)
O3sSC	0.43	0.20	−0.08	(0.59)
O3SC	0.40	0.15	−0.06	[0.45]

without it (correlations 0.54, 0.60, and 0.58). This negative influence on Nordeste hindcasting does not appear in the midtropospheric correlations of Table 6a but may be present in the surface temperature correlations of Table 7a.

Usually, almost 90% of Zimbabwe's annual rainfall occurs in the months of November to March. The AGCM hindcasts over Zimbabwe are therefore compared to observations in terms of

Table 7b. Regional Correlations of AGCM and GISTEMP Surface Air Temperature Time Series, Seasonal 1979–1995

Run	Nordeste 4°S–12°S 37°W–48°W				NH Land			
	DJF	MAM	JJA	SON	DJF	MAM	JJA	SON
<i>SST Forcing</i>								
SST a	0.28	0.37	0.64	0.38	0.25	0.06	0.53	0.21
SST b	0.22	0.42	0.41	0.25	0.30	0.23	0.45	0.55
SST c	0.34	0.42	0.38	0.20	0.30	0.32	0.17	0.57
SST d	0.41	0.40	0.29	0.24	0.04	0.17	0.22	0.57
SST e	0.25	0.45	0.46	0.43	0.29	0.19	0.30	0.48
SST f	0.19	0.40	0.61	0.28	0.28	−0.01	0.02	0.32
SST g	0.33	0.56	0.49	0.33	0.19	0.26	0.07	0.45
SST mean	0.29	0.43	0.47	0.30	0.23	0.17	0.25	0.45
SST std	0.08	0.06	0.12	0.08	0.09	0.12	0.19	0.14
<i>SST Ensemble</i>								
SST ag	0.38	0.56	0.63	0.38	0.35	0.33	0.50	0.65
<i>Atmospheric Forcing</i>								
GG	0.19	0.41	0.30	0.41	0.09	0.16	0.11	0.50
VOL	0.24	0.43	0.37	0.24	0.29	0.37	([0.49])	0.58
O3s	0.25	0.44	0.33	0.26	(0.50)	0.34	0.33	0.40
O3t	(0.08)	(0.26)	0.42	0.33	0.24	0.35	(0.47)	0.54
O3	(0.09)	0.39	0.40	([0.57])	0.29	0.39	(0.56)	0.46
O3sS	0.27	0.48	0.51	0.25	0.33	0.34	0.42	0.53
O3sSC	0.21	0.48	0.50	0.31	0.25	(0.45)	([0.62])	0.62
O3SC	0.17	0.41	0.43	(0.48)	0.26	[0.20]	[0.39]	0.57

these 5 months of precipitation anomalies over 1979–1997. Correlations between the AGCM rainfall and station data, however, are poor or negative over Zimbabwe for all of the runs. The average SST ag, for example, has a correlation of 0.15. Similarly, rainfall over the U.S. Corn Belt is uncorrelated with observations. This is unsurprising, considering that the chaotic nature of midlatitudes prevented any significant correlation between model and observed midtropospheric temperatures in this agricultural region.

However, North American seasonal precipitation responses have been documented. *Ropelewski and Halpert* [1986] identified typical spatial patterns of North American precipitation and temperature anomalies tied with the ENSO cycle. The southeastern United States and northern Mexico had positive precipitation anomalies for 18 of 22 warm events. Composites of U.S. precipitation anomalies for seven ENSO warm events by *Livezey et al.* [1997] similarly showed that January through March had anomalous rain along the Gulf Coast from Texas to Florida. In addition, these months, particularly January, experience large negative precipitation anomalies over the U.S. Midwest and Lower Mississippi Valley (excluding Louisiana). *Wang et al.* [1999] also found correlations between warm Pacific SST anomalies and positive winter precipitation anomalies for southern California eastward to Texas. Cold Pacific SST anomalies, on the other hand, were correlated with drought in the southeast United States and rainy conditions in the Midwest.

Therefore patterns of the simulated December–February (DJF) precipitation anomalies over North America are examined from the SST-forcing average, SST ag. Such precipitation anomalies are relevant to the U.S. winter wheat crop. Rain gage data (not shown) of the DJF 1982–1983 El Niño season has large positive rainfall anomalies of 100–200 mm across the Pacific and Gulf coasts and a strip of heavy rainfall from the Mississippi Valley delta northward. The northeastern United States and Ohio Valley experience significant negative precipitation anomalies. Negative departures in the Ohio Valley overlap the area of below-normal precipitation identified by *Livezey et al.* [1997] in El Niño composites of January–March. Positive anomalies over the southeastern United States and

Table 8. Regional Correlations of AGCM and NCDC 5-Month-Smoothed Precipitation Time Series, 1979–1997

Run	Nordeste 4°S–12°S 37°W–48°W
SST a	0.41
SST b	0.50
SST c	0.63
SST d	0.54
SST e	0.40
SST f	0.42
SST g	0.54
SST mean	0.49
SST std	0.09
SST ag	0.59
GG	0.54
VOL	0.38
O3s	0.54
O3t	0.49
O3	0.43
O3sS	0.60
O3sSC	0.58
O3SC	0.48

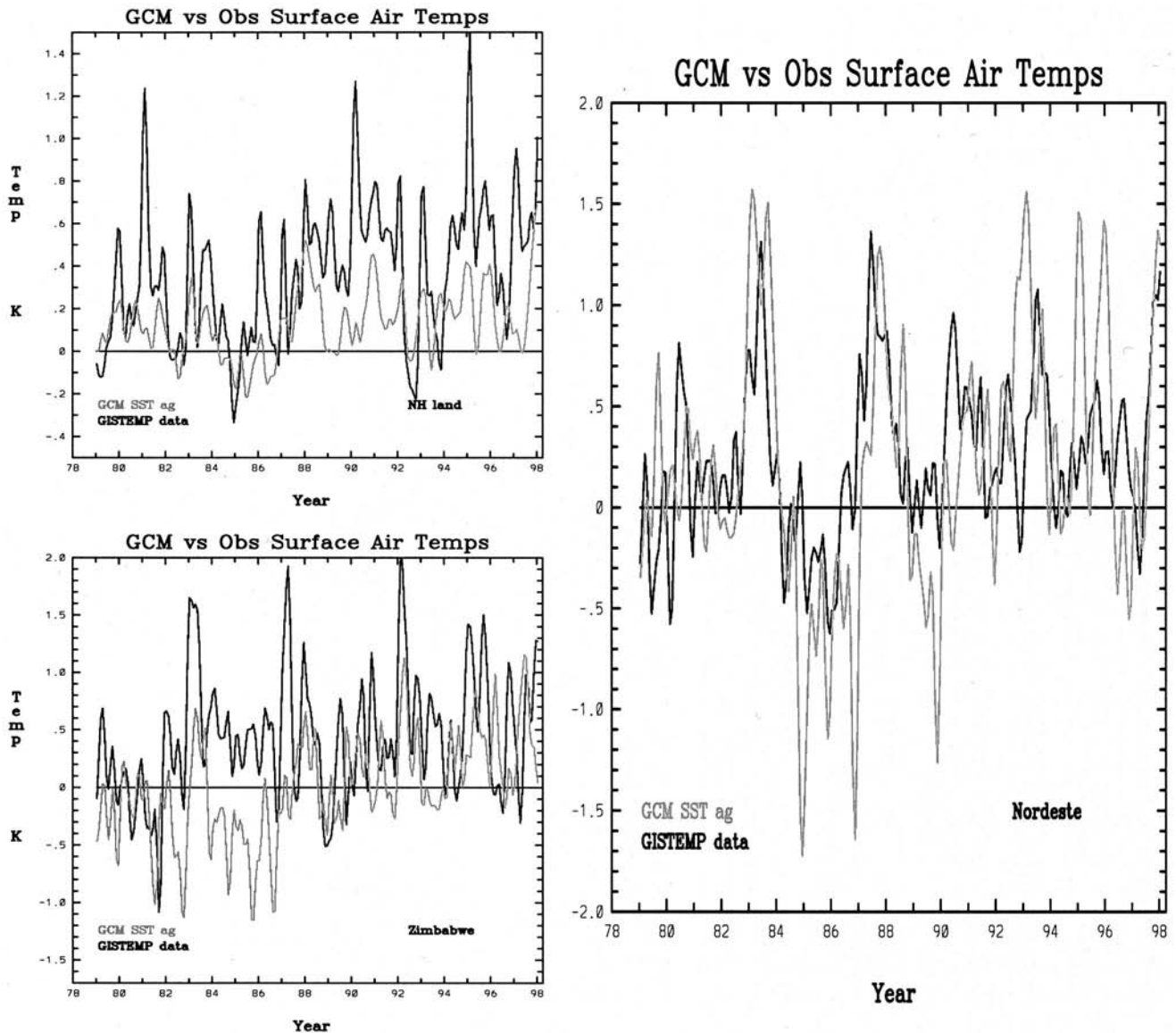


Figure 7. Agreement between smoothed surface air temperatures from meteorological station data and from the average climate of seven AGCM runs, SST ag, are shown over Northern Hemispheric land (top left), Zimbabwe (bottom left), and Nordeste (right). Smoothing over 3 months has been applied to these time series.

near the Pacific coast occur in the AGCM average, SST ag, (Figure 8), but the ensemble does not simulate negative rainfall anomalies over northeastern United States and Ohio Valley.

The La Niña season of DJF 1988–1989 featured drought along the Gulf, Atlantic, and Pacific coasts. A single contiguous area of excessive rainfall extended from the Mississippi Valley northeastward into the Tennessee and Ohio Valleys. The AGCM SST ensemble, SST ag, does have a drier regime over the Gulf and along the Pacific Coast which overlaps areas of the observed drought. It does not simulate the dry conditions along the east coast or the heavy rains observed in Tennessee/Kentucky (see Figure 8).

5. Summary

Multiple realizations of the 1969–1998 time period have been hindcast by the GISS AGCM to examine its performance over wide zonal bands and over sensitive agricultural regions.

While the initial ensemble of seven runs was only forced by SSTs, subsequent runs incorporated atmospheric forcings from greenhouse gases, stratospheric volcanic aerosols opacities, stratospheric ozone, sparsely observed tropospheric ozone, and even more poorly observed tropospheric sulfate and black carbon aerosols. Several questions can be answered as follows:

1. Does the AGCM simulate the midtropospheric temperature dumbbell pattern of Yulaeva and Wallace [1994] in response to El Niño SST forcing? Yes. However, the AGCM warmings in the troposphere do not always occur in discrete, off-equator centers as observed. Does the AGCM tropopause move and the stratospheric temperatures cool and compensate locally for tropospheric warmth during El Niño [Reid *et al.*, 1989; Yulaeva and Wallace, 1994; Randel and Cobb, 1994]? Yes. Despite the coarse vertical resolution of this nine-layer AGCM, its lower stratospheric temperatures do respond locally to the El Niño SST anomalies with cool anomalies over the eastern Pacific.

AGCM Precipitation: El Niño vs La Niña

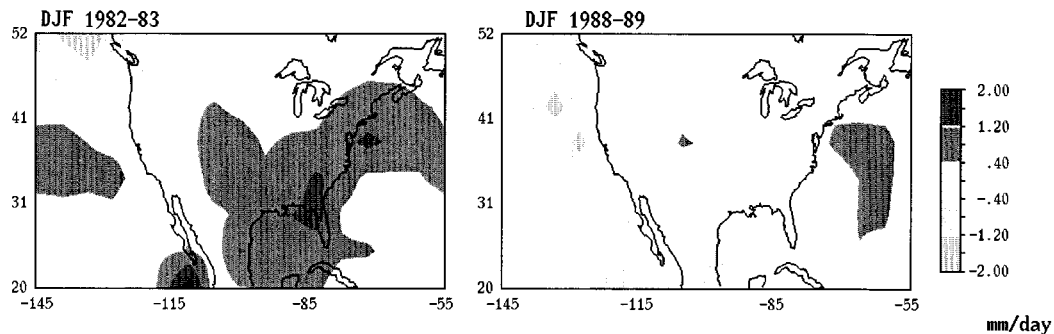


Figure 8. Precipitation anomalies for the December–February (DJF) of the 1982–1983 El Niño and 1988–1989 La Niña are shown over North America from the average of the seven SST-forced AGCM runs, SST ag.

2. Is there reduced static stability in the tropical upper troposphere over the Pacific due to warm equatorial SST? Yes. Do the upper tropospheric, subtropical jet stream, and the Hadley Cell circulation strengthen promoting teleconnections? Yes. In January 1983 and January 1998, for instance, the upward vertical motion in the southern branch of the Hadley cell tripled, its associated stream functions increased by up to 18%, the associated meridional flow in the upper troposphere increased in speeds by up to 13%, and the subtropical jet zonal wind speeds increased by up to 12%.

3. How well can the AGCM correlate with the oceanic lower tropospheric, midtropospheric, and lower stratospheric temperature time series of MSU? Correlations for 1979–1998 between 3-month-smoothed AGCM and MSU temperature time series reach 0.93 globally for the lower stratosphere, 0.66 globally and 0.84 in the tropics for the midtroposphere, and 0.61 globally and 0.79 in the tropics for the oceanic lower troposphere. Correlations of lower tropospheric T_b may have been systematically lowered by the use of mean sea ice coverage in the AGCM runs. The AGCM consistently disagreed with warm, lower tropospheric MSU anomalies prior to mid-1981 reminiscent of concerns with anomalous MSU channel 2R discontinuities found by Hurrell and Trenberth [1998] in comparisons of MSU to SST observations.

4. Do the correlations improve with additional atmospheric forcings? Yes and no. Correlations over latitudinal zones improve significantly in the lower stratosphere and in the midtroposphere but less so in the lower troposphere over oceans. Plate 3 shows the MSU and AGCM time series from the runs forced by the most certain observations, greenhouse gases, volcanic aerosols, and stratospheric ozone. Tropospheric T_b anomalies during warm El Niño events, in particular, achieve warmer responses, more favorable for resultant teleconnections. This least uncertain collection of atmospheric forcings also yields most of the top correlations for the lower stratospheric, midtropospheric, and lower tropospheric temperatures and for surface air temperatures and precipitation anomalies. Hansen *et al.* [1995, 1996b, 1997] and Folland *et al.* [1998] found similar improvement in AGCM upper air temperatures with the inclusion of stratospheric volcanic aerosols and ozone forcings.

This result is complicated by the land-ocean bias of AGCM responsiveness to imposed atmospheric forcings on top of specified SSTs: ocean-dominated, Southern Hemispheric correlations are relatively indifferent to imposed atmospheric

forcings, while the land-dominated Northern Hemispheric correlations respond to imposed atmospheric forcings. Southern Hemispheric correlations between the AGCM and observations remain less than their Northern Hemispheric counterparts. Only lower stratospheric T_b correlations are similar in both the Northern and the Southern Hemispheres and equally responsive to the addition of known atmospheric forcings.

Comparisons between the individual atmospheric forcings is difficult, given single hindcasts, the varying land amounts in latitudinal zones, the differing regional and vertical distributions of the forcings, and the AGCM redistribution of the impact of a forcing. For instance, while stratospheric ozone depletion is specified primarily in the middle to high latitudes, the AGCM tropospheric temperatures improve across equatorial latitudes. In another example, runs adding tropospheric ozone forcing either saw unchanged temperature correlations, with a background of SSTs, greenhouse gases, volcanic aerosols and stratospheric ozone forcings, or saw significantly lower-temperature correlations, with a background of the penultimate combination of atmospheric forcings. Similar experiments by Folland *et al.* [1998] used comparisons with radiosonde upper air temperatures and had found strong improvement with inclusion of tropospheric ozone changes. This variable impact from inclusion of tropospheric ozone opens the door to questions concerning the necessity of the presence of another forcing in order to obtain the desired outcome or hindcast. Addition of greenhouse gas forcing onto SST forcing, for example, actually lowered midtropospheric temperature correlations significantly, apparently unbalanced without the presence of other observed forcings.

5. How good is the AGCM response over sensitive agricultural regions? The AGCM midtropospheric temperature response is quite good over Nordeste, northeastern Brazil, at maximum correlation with observations of 0.75, moderate over Zimbabwe at 0.54, and weak over the U.S. Corn Belt at 0.25. The latter two agricultural regions, in Africa and in the northern midlatitudes, suffered from higher levels of non-SST variability. Finally, does the AGCM response over these agricultural regions improve with inclusion of atmospheric forcings? The AGCM response remains mostly the same over the agricultural regions irrespective of the introduced atmospheric forcings. Only the combination of greenhouse gases, volcanic aerosols, and stratospheric ozone depletion (run O3s) seem to provide surface air temperature and precipitation anomalies over Zimbabwe notably better than the SST-forced ensemble.

Table 9. Impact of AGCM Ensemble Size on Unsmoothed Time Series Correlations With Observations, 1979–1998

Variable	SST ag r 7 Runs	SST ae r 5 Runs	SST ac r 3 Runs	SST a r 1 Run
Ch 2 T_b				
Glob	0.57	0.56	0.55	0.56
NH	0.57	0.57	0.56	0.40
SH	0.38	0.36	0.34	0.30
NH ml	0.36	0.35	0.30	0.15
Nordeste	0.72	0.73	0.71	0.58
Zimbabwe	0.33	0.30	0.28	0.19
Oceanic Ch 2R T_b				
Glob	0.50	0.49	0.49	0.47
NH	0.56	0.56	0.56	0.40
SH	0.30	0.28	0.27	0.30
NH ml	0.51	0.50	0.47	0.41
Surf air T				
NH land	0.42	0.42	0.40	0.22
Nordeste	0.38	0.36	0.35	0.31
Zimbabwe	0.14	0.12	0.10	0.00

The AGCM hindcasts do have a seasonal dependence. The Nordeste midtropospheric temperatures from the AGCM match observations best in the winter (JJA) and spring (SON) with maximum midtropospheric correlations of 0.76 and 0.74, respectively. Surface temperature time series match GISTEMP observations best during the winter (JJA) at 0.64 and fall (MAM) at 0.56 for Nordeste and during the summer (JJA) at 0.62 and fall (SON) at 0.62 for Northern Hemispheric land. As crop production over the United States relies on germination and establishment during the spring (MAM) months and tasseling and grain fill during the summer months (JJA), the stronger performance during the Northern Hemispheric land summer is encouraging. Each region encompasses six AGCM grid cells and, while atmospheric forcings improve hindcasts over hemispheric or zonal areas, the space of six grid cells is susceptible to variability and more sensitive to synoptic mechanisms. For hindcasts or forecasts over such small areas, this AGCM diagnostics should probably be used to initialize and update regional models whose diagnostics could then be given to agricultural, fishery, and economic models.

In future work the influence of higher vertical and horizontal resolution in the climate model will be examined. Also, the number of runs needed with varying resolution for a sound ensemble average will be addressed. Table 9 shows the impact on correlations with observations when the number of runs varies from one to seven. For this AGCM it appears that five runs may have sufficed for temperature hindcasts from the SST ensemble. This result echoes work by *Stendel and Bengtsson* [1997] who examined the average of five simulations from the Hamburg climate model (ECHAM) forced only by SSTs and found sufficient agreement between the model and the MSU channel 2r time series over 1979–1993 in the tropics and over oceans. The failure of the observed SST forcing to prompt the AGCM to produce high correlations in the Southern Hemisphere suggests that the specified SST data may be wrong in areas. This is certainly possible given the sparseness of such observations particularly over southern middle to high latitudes and may be addressed by future AMIP SST prescriptions. Forcings due to solar variability and the QBO will also be incorporated into future work. Finally, the CAFE project plans to run these forcing experiments in three lower boundary conditions: for the “ideal” match with use of observed sea surface

temperatures (SSTs) and observed sea ice extent; for the “less-than-ideal” match of OAGCM-calculated SSTs and sea ice; and for the “forecasting” mode into the early 2000s. These different phases would test the capability of an interactive ocean to produce the observed SST trends given the atmospheric forcings.

Appendix: AGCM, Forcings, and Microwave Radiative Transfer Model

Table 1 lists the GISS CAFE AGCM runs and their applied forcings. The seven SST-forced runs (SST a–SST g) differ in terms of their initial conditions and act individual realizations of the 1969–1998 period. Subsequent climate model runs have explicit atmospheric forcings added in cumulatively. All of the runs in Table 1 have sea ice coverage specified climatologically due to issues over the spatial and temporal continuity of current sea ice datasets. The sea ice coverage is based on the 1979–1993 period and the version released for usage with the Atmospheric Model Intercomparison Project I (AMIP I) but with slight modifications.

A1. AGCM

The AGCM version employed is roughly referred to as “SI96” as it includes model development for the 1996 GISS “Summer Institute.” The coarse resolution of nine vertical layers and 4° latitude by 5° longitude works with a quadratic upstream scheme for moisture and heat advection and a fourth-order scheme for momentum advection. Both of these schemes imply finer resolution for horizontal and vertical advection. The rigid top of the AGCM occurs in the lower stratosphere at roughly 31 km or 10 mbar (see Figure 1). This climate model has the typical collection of climate feedback parameterizations, such as cloud formation and snow cover. The cloud parameterizations are described by *Del Genio et al.* [1996], the land surface parameterizations by *Rosenzweig and Abramopoulos* [1997], and the planetary boundary layer by *Hartke and Rind* [1997]. The radiation package employed by the AGCM has compared quite well with line-by-line calculations and with radiation code in other AGCMs [*Cess et al.*, 1993]. The SI96 version of the AGCM differs from the SI95 version used by *Hansen et al.* [1997] only in a newer cloud scheme; an improved orbital calculation of solar irradiation and an associated solar constant change to 1367 W/m² from 1362 W/m²; small changes of increasing puddling on sea ice, snow melting before ice, and associated hydrology adjustments; increased radiation time steps; additional dependence on surface type for radiation fluxes; and consolidation of relationships among cloud cover, threshold relative humidity, and background relative humidity to reduce unwanted shortwave absorption in middle and high latitudes.

A2. Forcings

The SSTs used to force the climate model are monthly values from the analysis of *Reynolds and Smith* [1994]. Their data set was distributed at 2° by 2° resolution and so was interpolated to the necessary 4° by 5° grid size using the ETOPO5 data set as a land reference. The monthly sea surface temperature anomalies inherently contain some portion of the atmospheric forcings. Figure A1 shows the SSTs after a 3-month smoothing across the tropical Pacific, the Northern Hemisphere, and the Southern Hemisphere. The Northern

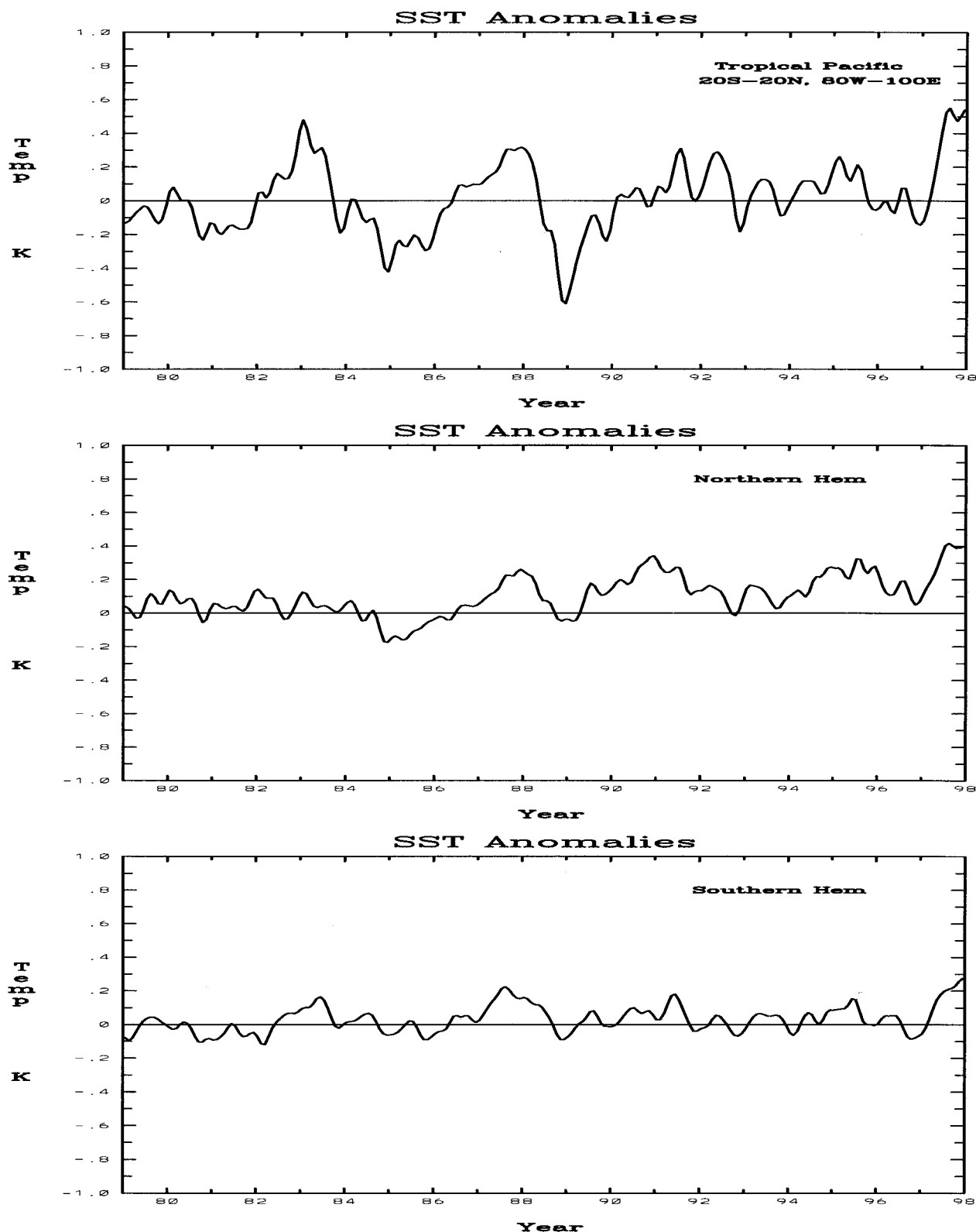


Figure A1. Specified sea surface temperatures used to force the AGCM are shown as 3-month-smoothed time series averaged over (top) the tropical Pacific (20°S–20°N and 80°W–100°W), (middle) the Northern Hemisphere, and (bottom) the Southern Hemisphere.

Hemispheric averages, in particular, show a warming trend perhaps derived from anthropogenic forcing.

The explicit atmospheric forcings begin in AGCM run GG with observed variation in greenhouse gas forcings by CO₂,

CH₄, N₂O, CFC-11, and CFC-12. The specified CO₂ increases are similar to observations and IPCC scenarios [IPCC, 1992]. Increases match observations up to 1994. Then increases are annual fixed rates dependent on the particular gas. Table A1

lists the trace gas concentrations used to force the experiments. While the CO_2 increases are uniform with height, the other trace gases only increase up to 16 km and, at higher levels, have diminishing increases with a 10 km scale height.

AGCM run VOL adds in zonal stratospheric aerosol optical depth forcings [Sato *et al.*, 1993; Hansen *et al.*, 1996b] seen in Figure A2. These aerosol optical depths change the net radiation entering the troposphere and warm in situ stratospheric temperatures, affecting dynamics. This stratospheric warming is clearly seen in the MSU channel 4 T_b time series of Plate 3. A background optical depth of 0.0001 serves as a lower limit for aerosol forcing after 1979. The optical depths were derived from the Stratospheric Aerosol and Gas Experiment (SAGE) occultation data available from 1979 to 1980 and then 1985 onward, as detailed by Hansen *et al.* [1996b]. SAGE occultation data were not available after the 1982 El Chichón eruption and the optical depths of Sato *et al.* [1993] with a 10% increase based on comparison with multiple data analyses [Hansen *et al.*, 1996b; Hansen *et al.*, 1997]. Optical depths due to the 1991 Pinatubo eruption were derived via four wavelength measurements in the solar occultation data by SAGE II with extrapolations applied during saturation events and with constraints from 12.1 μm Improved Stratospheric and Mesospheric Sounder (ISAMS) measurements [Hansen *et al.*, 1996b]. The optical depths for the January 1995 to December 1999 period were extrapolated assuming an exponential decay with a time constant of 1 year across all latitudes. Figure A2 shows that the resultant optical depth forcing at 0.55 μm peaks at 0.30 in northern tropical latitudes after the 1982 El Chichón eruption, with an associated global mean maximum of 0.09, and peaks at 0.26 just south of the equator after the 1991 Mount Pinatubo eruption, with an associated global mean maximum of 0.15.

Severe ozone depletion has occurred in the lower stratosphere and upper troposphere from 1970 onward. Loss occurred most deeply in ambient ozone abundances near 17 km with trends of -1.5 to -3% per year from February 1979 to April 1991 [McCormick *et al.*, 1992]. These negative trends were near zero at the equator but increased toward the poles with strongest values in the Southern Hemisphere spring [Stolarski *et al.*, 1991]. Randel and Cobb [1994] found strong positive correlations between MSU lower stratospheric channel 4 T_b and total ozone column data from TOMS. Hansen *et al.* [1995], in turn, found ozone cooling of the surface air level

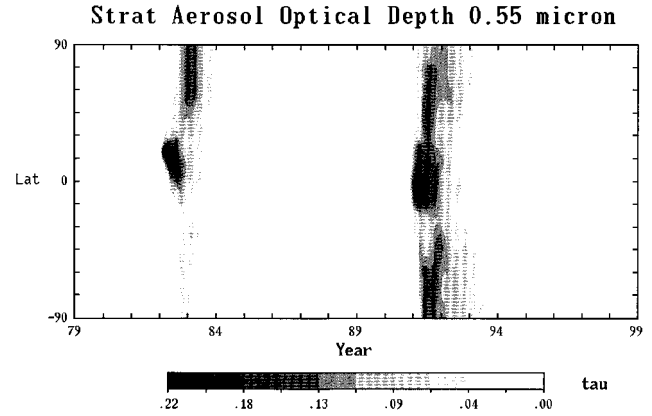


Figure A2. Stratospheric volcanic aerosols used to force the AGCM are shown in terms of the optical depth at 0.55 μm over the 1979–1999 period and over all latitudes.

(0.03°C/decade) to be less than cooling in the lower troposphere at 800 mbar (0.06°C/decade) with their idealized-geography climate model.

The AGCM background levels of ozone is based on the ozone climatology of McPeters [1993] which are 1979–1980 levels. Zonal stratospheric ozone trends have already been derived from the Solar Backscatter Ultraviolet (SBUV) measurements of ozone total column amounts and profiles above 32 mbar [Hollandsworth *et al.*, 1995] and the SAGE stratospheric ozone profiles between 125 and 32 mbar [McCormick *et al.*, 1992] by Hansen *et al.* [1997]. AGCM run O3s adds in such stratospheric ozone trends. Figure A3 shows the total ozone change from its specified zonal inputs and the ozone time series at different pressure levels over Washington, D. C. (38°N).

The tropospheric ozone changes added separately into AGCM run O3t are much more uncertain than the stratospheric ozone changes. Tropospheric ozone levels, roughly 10% of the total column ozone amount, are specified geographically as shown in Figure A3c. Specified ozone increases occur primarily in the midtroposphere and across the Northern Hemisphere by up to 20 Dobson units (DU) since the pre-industrial year 1850 and by up to 8 DU between 1995 and 1970 [Hansen *et al.*, 1997]. This Northern Hemispheric enhancement agrees with IPCC estimates [IPCC, 1996], but the Southern Hemispheric changes of Figure A3c are not negative over the southern high latitudes as suggested by IPCC. Rates of increase for the tropospheric ozone forcing remain fixed after 1985 in rough agreement with observations showing slowing or stopping of its upward trend [IPCC, 1996]. Tropospheric ozone observations are sparse. Therefore the global and vertical tropospheric ozone changes of Figures A3c and 3d have little regional or fine-scale structure. AGCM run O3 has both the tropospheric and the stratospheric ozone forcings included.

Tropospheric aerosols are the last added atmospheric forcing in Table 1 and the most uncertain in terms of background distribution and trends. Their distributions, despite a short lifetime of a few days in the troposphere, arise from continual combustion of fossil fuels, biomass burning, desert dust uplift, and other sources. Sulfur aerosols, in run O3sS, and black carbon (soot) aerosols, in run O2sSC, force the AGCM radiation package. The indirect impact of tropospheric aerosols

Table A1. Trace Gas Concentrations Used As AGCM Forcings

Year	CO_2 ppm	N_2O ppb	CH_4 ppb	CFC-11 ppt	CFC-12 ppt
1969	323.4	294.4	1389.7	51.1	106.5
1972	327.0	296.2	1429.7	78.1	150.0
1975	330.7	298.0	1475.5	116.0	207.0
1978	334.6	300.4	1522.7	147.4	257.1
1981	341.3	303.4	1581.0	283.5	330.5
1984	345.7	305.8	1620.0	445.0	383.0
1987	350.1	306.8	1659.0	612.5	436.0
1990	354.8	309.8	1687.0	780.0	489.5
1993	357.9	312.0	1709.0	928.5	524.0
1996	362.2	313.9	1737.0	1065.5	528.0
1999	366.4	315.7	1761.0	1185.5	528.0

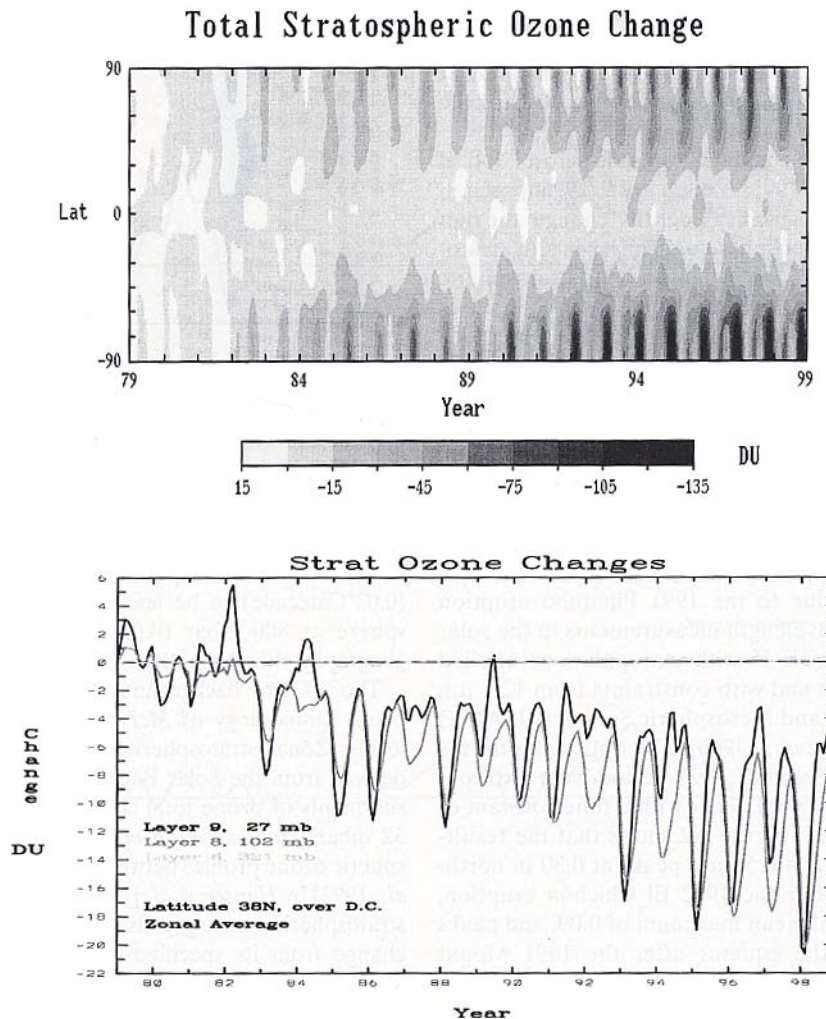


Figure A3. Ozone changes used to force the AGCM are shown: (a) the zonal stratospheric ozone forcings in terms of the total ozone change over 1979–1999 and all latitudes; (b) the zonal stratospheric ozone forcing in terms of its time series for three pressure levels from 1979 to 1999; (c) the tropospheric ozone increase over latitude and longitude in terms of the total Dobson unit (DU) from 1970 to 1995; and (d) tropospheric ozone increases over latitude in terms of pressure levels zonally and annually averaged for AGCM layers centered on 321, 633, and 894 mbar.

influencing cloud condensation nuclei is not incorporated. While scattering of tropospheric sulfuric aerosols cools local temperatures, tropospheric soot aerosols absorb radiation and primarily warm local temperatures. Background sulfur distributions were provided by D. Koch [Koch *et al.*, 1999] and a background carbon distribution by I. Tegen (personal communication, 1999). The 1970 and 1995 December geographical distributions of sulfuric and soot tropospheric aerosols are shown in Figure A4. Trends for sulfuric aerosols are specified in nine regions from 1950 to the present and are based on CO₂ emissions (A. D. Robertson *et al.*, manuscript in preparation, 1999). Thus the United States, Europe, and eastern Asia have stronger emission rates than Africa. Given the fewer observations available on tropospheric soot aerosols, these sulfuric trends are applied to the background soot distribution.

The last AGCM run, O3SC, has all of the atmospheric forcings applied (see Table 1). The AGCM run, O3s, incorporates the least uncertain forcings since it excludes tropospheric ozone and tropospheric aerosols from its specified forcings.

A3. Microwave Radiative Transfer Model

The microwave radiative transfer model produces brightness temperatures based on the AGCM monthly-mean global fields of atmospheric and surface diagnostic parameters. T_b calculations assume a nonscattering, refracting atmosphere containing absorbing molecular oxygen and water vapor in local thermodynamic equilibrium above a spectrally gray, Lambertian surface. Nonnegligible scattering from precipitation and large convective ice particles is ignored as such scattering events were filtered out of the MSU climatologies.

Interaction with the surface is characterized by an emissivity. Snow-free land has the highest emissivity of 1.0, snow-covered land an emissivity of 0.85, ice-covered oceans an emissivity of 0.70, and oceans an emissivity of 0.50. The snow-free land provides a very warm background and the oceans a cold background for microwave channels sensitive to the surface. In the tropics, roughly 20% of the full signal or 58 K comes from surface emission over land and 10% or 29 K from surface emission over ocean for lower tropo-

spheric channel 2R T_b [Shah and Rind, 1995]. Changing the surface emissivity by 0.1 alters channel 2 T_b by 0.4 K and channel 2R T_b by 0.8 K over tropical low-topography areas. For this reason, channel 2R values from the AGCM are masked over land and only values over the less variable ocean surfaces are considered. Channel 2 T_b values are similarly masked over high topography, the Himalayas, the Andes, the Greenland Plateau, and Antarctica.

This microwave postprocessor has favorably contrasted radiosonde and the NCEP/NCAR reanalysis climatologies with the MSU tropospheric and stratospheric monthly mean climatologies [Shah and Rind, 1998]. It has also produced zenith attenuations in agreement with available observations [Shah and Rind, 1995]. While Hansen et al. [1995, 1997] used a quicker weighting functions method to calculate MSU T_b from AGCM diagnostics, the full radiative transfer model is employed herein to ensure sensitivity to changing profiles of temperature, humidity, and refraction and to changing snow and ice coverage. The microwave radiation code is available from K. Shah.

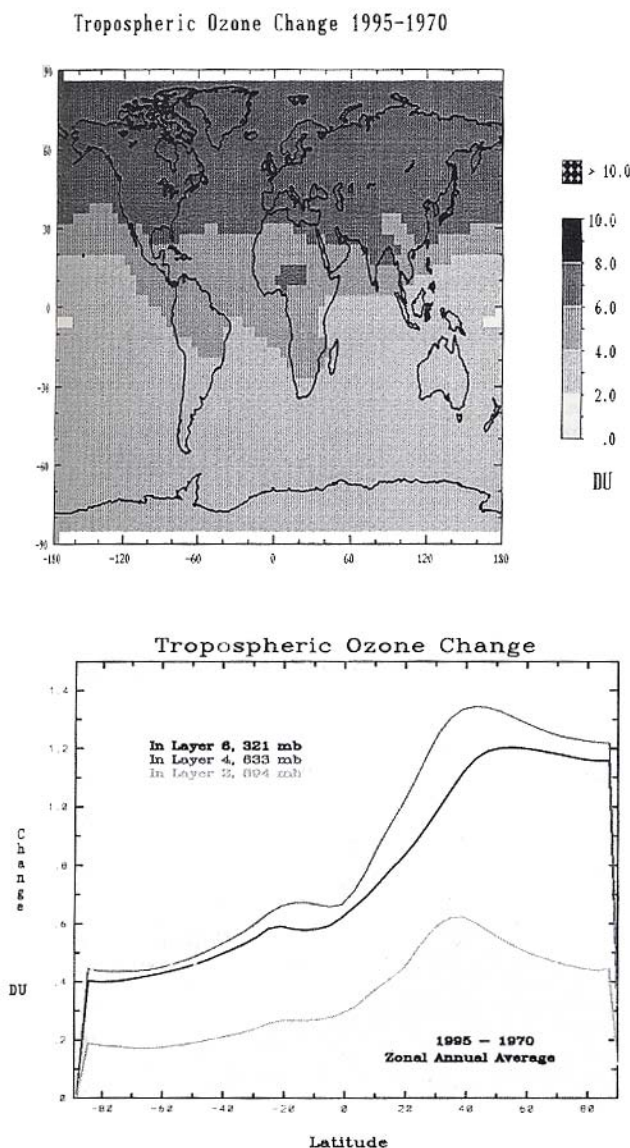


Figure A3. (continued)

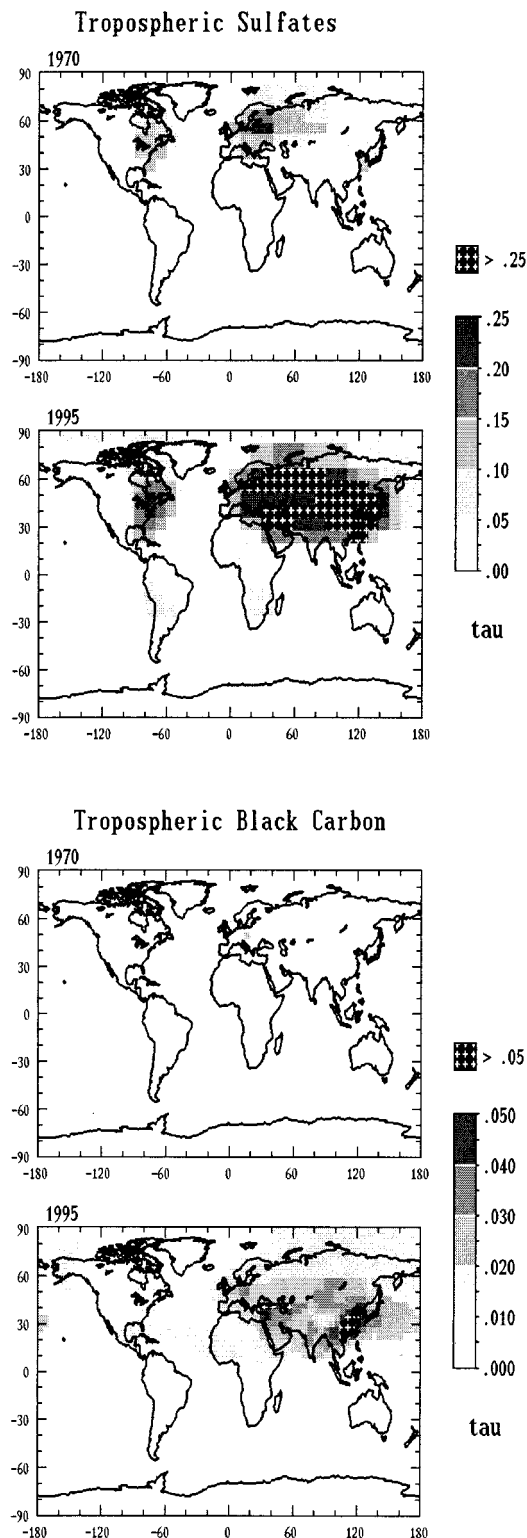


Figure A4. Sulfur and black carbon (soot) tropospheric aerosol optical thicknesses, tau at $0.55 \mu\text{m}$, and their geographical distributions are shown for December 1970 and 1995.

Acknowledgments. The CAFE work was supported by a NASA Earth System Science grant NCC5-117. K. Shah was also supported by NSF grant ATM-96-28843. L. Druyan was also supported by NSF grant ATM-97-25142. NASA GISS climate work was also supported by NASA Climate and Earth Observing System Programs. Nordeste precipitation data were generously supplied by L. Greischar and S. Hastenrath.

References

- Boyle, J. S., Intercomparison of interannual variability of the global 200-hPa circulation for AMIP simulations, *J. Clim.*, **11**, 2505–2529, 1998.
- Cane, M. A., G. Eshel, and R. W. Buckland, Forecasting Zimbabwe maize yield using eastern equatorial Pacific sea surface temperature, *Nature*, **370**, 204–205, 1994.
- Cess, R. D., et al., Uncertainties in carbon dioxide radiative forcing in atmospheric general circulation models, *Science*, **262**, 1252–1255, 1993.
- Christy, J. R., R. W. Spencer, and E. S. Lobl, Analysis of the merging procedure for the MSU daily temperature time series, *J. Clim.*, **11**, 2016–2041, 1998.
- Chu, P., Brazil's climate anomalies and ENSO, in *Teleconnections Linking Worldwide Climatic Anomalies*, edited by M. Glantz, R. Katz, and N. Nicholls, pp. 43–72, Cambridge Univ. Press, New York, 1991.
- Del Genio, A. D., M.-S. Yao, W. Kovari, and K.-W. Lo, A prognostic cloud water parameterization for global climate models, *J. Clim.*, **9**, 270–304, 1996.
- Druryan, L., K. Shah, M. Chandler, and D. Rind, GCM hindcast of SST-forced climate variability over agriculturally intensive regions, *Clim. Change*, **45**, 279–322, 2000.
- Folland, C. K., D. M. H. Sexton, D. Karoly, C. Johnson, D. Rowell, and D. Parker, Influences of anthropogenic and oceanic forcings on recent climate change, *Geophys. Res. Lett.*, **25**, 353–356, 1998.
- Gaffen, D., Falling satellites, rising temperatures?, *Nature*, **394**, 615–616, 1998.
- Hansen, J., et al., Efficient three-dimensional global models for climate studies: Models I and II, *Mon. Weather Rev.*, **111**, 609–662, 1983.
- Hansen, J., H. Wilson, M. Sato, R. Ruedy, K. Shah, and E. Hansen, Satellite and surface temperature data at odds?, *Clim. Change*, **30**, 103–117, 1995.
- Hansen, J., et al., A Pinatubo climate modeling investigation, in *The Mount Pinatubo Eruption, Effects on the Atmosphere and Climate*, edited by G. Fiocco, D. Fua, and G. Visconti, *NATO ASI Ser.*, **1**(42), 233–272, 1996a.
- Hansen, J., R. Ruedy, M. Sato, and R. Reynolds, Global surface air temperatures in 1995: Return to pre-Pinatubo levels, *Geophys. Res. Lett.*, **23**, 1665–1668, 1996b.
- Hansen, J., et al., Forcings and chaos in interannual to decadal climate change, *J. Geophys. Res.*, **102**, 25,679–25,720, 1997.
- Hansen, J., M. Sato, R. Ruedy, A. Lacis, and J. Glascoe, Global Climate Data and Models: A reconciliation, *Science*, **281**, 930, 1998.
- Hansen, J., R. Ruedy, J. Glascoe, and M. Sato, GISS analysis of surface temperature change, *J. Geophys. Res.*, **104**, 30,997–31,022, 1999.
- Hartke, G., and D. Rind, Improved surface and boundary layer models for the GISS GCM, *J. Geophys. Res.*, **102**, 16,407–16,422, 1997.
- Hastenrath, S., and L. Greischar, Further work on the prediction of Northeast Brazil rainfall anomalies, *J. Clim.*, **6**, 743–758, 1993.
- Hoerling, M. P., and A. Kumar, Origins of extreme climate states during the 1982–83 ENSO winter, *J. Clim.*, **10**, 2859–2870, 1997.
- Hoerling, M. P., A. Kumar, and M. Zhong, El Nino, La Nina and the nonlinearity of their teleconnections, *J. Clim.*, **10**, 1769–1786, 1997.
- Hollandsworth, S. M., R. D. McPeters, L. E. Flynn, W. Planet, A. J. Miller, and S. Chandra, Ozone trends deduced from combined Nimbus 7 SBUV and NOAA-11 SBUV/2 data, *Geophys. Res. Lett.*, **22**, 905–908, 1995.
- Hurrell, J., and K. Trenberth, Difficulties in obtaining reliable temperature trends: Reconciling the surface and satellite microwave sounding unit records, *J. Clim.*, **11**, 945–967, 1998.
- Inter (IPCC), *Climate Change*, 1992, edited by J. T. Houghton, B. A. Callander, and S. K. Varnay, Cambridge Univ. Press, New York, 1992.
- IPCC, *Climate Change*, 1995, edited by J. T. Houghton, L. G. Filho, B. A. Callander, N. Harris, A. Kattenberg, and K. Maskell, Cambridge Univ. Press, New York, 1996.
- Koch, D., D. Jacobs, I. Tegen, D. Rind, and M. Chin, Tropospheric sulfur simulation and sulfate direct radiative forcing in the GISS GCM, *J. Geophys. Res.*, **104**, 23,799–23,822, 1999.
- Lau, K.-M., J. H. Kim, and Y. Sud, Intercomparison of hydrologic process in AMIP GCMs, *Bull. Am. Meteorol. Soc.*, **77**, 2209–2228, 1996.
- Livezey, R., M. Masutani, A. Leetmaa, H. Rui, M. Ji, and A. Kumar, Teleconnective response of the Pacific-North American region atmosphere to large Central Equatorial Pacific SST anomalies, *J. Clim.*, **10**, 1787–1820, 1997.
- Kiladis, G. N., and H. F. Diaz, An analysis of the 1877–78 ENSO episode and comparison with 1982–83, *Mon. Weather Rev.*, **114**, 1035–1047, 1986.
- Matarira, C., Drought over Zimbabwe in a regional and global model, *Int. J. Clim.*, **10**, 609–625, 1990.
- McCormick, M. P., R. E. Veiga, and W. P. Chu, Stratospheric ozone profile and total ozone trends derived from the SAGE I and SAGE II data, *Geophys. Res. Lett.*, **19**, 269–272, 1992.
- McPeters, R. D., Ozone profile comparison, in *The Atmospheric Effects of Stratospheric Aircraft*, edited by M. J. Prather and E. E. Remsburg, *NASA Ref. Publ.* 1092, 1993.
- Phillips, J., B. Rajagopalan, M. Cene, and C. Rosenzweig, The role of ENSO in determining climate and maize yield variability in the U.S. Cornbelt, *Int. J. Climatol.*, **19**, 877–888, 1999.
- Prabhakara, C., R. Iacovazzi Jr., J.-M. Yoo, and G. Dalu, Global warming deduced from MSU, *Geophys. Res. Lett.*, **25**, 1927–1930, 1998.
- Press, W. H., B. P. Flannery, S. A. Teukolsky, and W. T. Vetterling, *Numerical Recipes, The Art of Scientific Computing*, Cambridge Univ. Press, New York, 1989.
- Randel, W. J., and J. B. Cobb, Coherent variations of monthly mean total ozone and lower stratospheric temperature, *J. Geophys. Res.*, **99**, 5433–5447, 1994.
- Reid, G. C., K. S. Gage, and J. R. McAfee, The thermal response of the tropical atmosphere to variations in equatorial Pacific sea surface temperature, *J. Geophys. Res.*, **94**, 14,705–14,716, 1989.
- Reynolds, R. W., and T. M. Smith, Improved global sea surface temperature analysis, *J. Clim.*, **7**, 929–948, 1994.
- Rind, D., J. Lerner, K. Shah, and R. Suozzo, Use of on-line tracers as a diagnostic tool in general circulation model development, *J. Geophys. Res.*, **104**, 9151–9167, 1999.
- Ropelewski, C. F., and M. S. Halpert, North American precipitation and temperature patterns associated with the El Nino-Southern Oscillation, *Mon. Weather Rev.*, **114**, 2352–2362, 1986.
- Ropelewski, C. F., and M. S. Halpert, Global and regional scale patterns associated with the El Nino/Southern Oscillation (ENSO), *Mon. Weather Rev.*, **115**, 2352–2362, 1987.
- Rosenzweig, C., and F. Abramopoulos, Land-surface model development for the GISS GCM, *J. Clim.*, **10**, 2040–2054, 1997.
- Sato, M., J. Hansen, M. P. McCormick, and J. B. Pollack, Stratospheric aerosol optical depths, 1850–1990, *J. Geophys. Res.*, **98**, 22,987–22,994, 1993.
- Shah, K. P., and D. Rind, Use of microwave brightness temperatures with a general circulation model, *J. Geophys. Res.*, **100**, 13,841–13,874, 1995.
- Shah, K. P., and D. Rind, Comparison of upper tropospheric and lower stratospheric temperatures: MSU, radiosonde, CIRA, and NCEP/NCAR reanalysis climatologies, *J. Geophys. Res.*, **103**, 31,569–31,592, 1998.
- Shindell, D. T., R. L. Miller, G. A. Schmidt, and L. Pandolfo, Simulation of recent northern winter climate trends by greenhouse-gas forcing, *Nature*, **399**, 452–455, 1999.
- Stendel, M., and L. Bengtsson, Toward monitoring the tropospheric temperatures by means of a general circulation model, *J. Geophys. Res.*, **102**, 29,779–29,788, 1997.
- Stolarski, R. S., P. Bloomfield, and R. D. McPeters, Total ozone trends deduced from Nimbus 7 TOMS data, *Geophys. Res. Lett.*, **18**, 1015–1018, 1991.
- Trenberth, K., General characteristics of El Nino-Southern Oscillation, in *Teleconnections Linking Worldwide Climate Anomalies*, edited by M. Glantz, R. Katz, and N. Nicholls, Cambridge Univ. Press, New York, 1991.
- Tribbia, J., The rudimentary theory of atmospheric teleconnections associated with ENSO, in *Teleconnections Linking Worldwide Climate Anomalies*, edited by M. Glantz, R. Katz, and N. Nicholls, Cambridge Univ. Press, New York, 1991.
- Wang, H., M. Ting, and J. Ming, Prediction of seasonal mean US precipitation based on El Nino SST, *Geophys. Res. Lett.*, **26**, 1341–1344, 1999.

- Wentz, F. J., and M. Schabel, Effects of orbital decay on satellite-derived lower tropospheric temperature trends, *Nature*, 394, 661–664, 1998.
- Wu, Z.-J., and B. McAvaney, Simulations of impacts of climatological MSU data processing methods using NCEP/NCAR reanalysis data, *J. Geophys. Res.*, 103, 19,495–19,508, 1998.
- Yulaeva, E., and J. M. Wallace, The signature of ENSO in global temperature and precipitation fields derived from the microwave sounding units, *J. Clim.*, 7, 1719–1736, 1994.
-
- M. Chandler, L. Druyan, D. Rind, and K. P. Shah, Center for Climate Systems Research, Columbia University, NASA Goddard Institute for Space Studies, 2880 Broadway, New York, NY 10025.
- P. Lonergan, Science Systems and Applications, New York, NY 10025.
- (Received June 5, 1999; revised October 28, 1999; accepted December 7, 1999.)